Chapter 4
Structural Characterization of Polymer Nanocomposites

Jayita Bandyopadhyay and Suprakas Sinha Ray

Abstract The performance of a heterogeneous material, such as polymer nanocomposites (PNCs) is dictated by three main factors: (i) the inherent properties of the components; (ii) interfacial interactions; and (iii) structure of the PNCs. The structure of a PNC depends on the dispersion and distribution of the nanoparticles (NPs) in the polymer matrix. However, improving the dispersion by mechanical means or via chemical bonding can influence the properties of the obtained PNCs. Therefore, elucidating the dispersion and distribution characteristics and the associated mechanisms is important and can allow prediction of the final properties. This chapter describes the different techniques used to characterize the structure and morphology of various PNCs. Primary techniques include microscopy in real space and reciprocal space, X-ray scattering analysis, as well as indirect measurements to probe the interfacial region and some physical properties. All the techniques mentioned here have certain pros and cons, but complement each other.

4.1 Introduction

Over the past decades, many efforts have been made to develop high-performance novel polymer-based materials by exploiting the benefits of polymer nanocomposite (PNC) technology. Various nano-fillers and polymers have been blended to achieve targeted properties for a particular application. However, it is obvious

---

J. Bandyopadhyay · S. Sinha Ray (✉)
DST-CSIR National Centre for Nanostructured Materials,
Council for Scientific and Industrial Research, Pretoria 0001, South Africa
e-mail: rsuprakas@csir.co.za

J. Bandyopadhyay
e-mail: jbandyopadhyay@csir.co.za

S. Sinha Ray
Department of Applied Chemistry, University of Johannesburg,
Doornfontein 2028, Johannesburg, South Africa
e-mail: ssinharay@uj.ac.za

S. Sinha Ray (ed.), *Processing of Polymer-based Nanocomposites*,
Springer Series in Materials Science 277,
https://doi.org/10.1007/978-3-319-97779-9_4

that the results do not always meet expectations. Therefore, elucidating the structure–property relationship of PNCs enables further understanding of the unique, but challenging, aspects of the materials. This chapter provides an overview of the different structural characterization techniques used to analyze PNCs. These methods can be categorized according to the table presented in Fig. 4.1 [1]. The reciprocal space scattering techniques are extremely powerful and enable analysis of the bulk properties of the material. On the other hand, microscopy techniques and tomography provide a direct view of the morphology and degree of the dispersion of the NPs in the polymer matrix. However, care must be taken to interpret the images correctly and avoid artefacts. The interfacial area can be analyzed by electron paramagnetic resonance (EPR), nuclear magnetic resonance (NMR), and optical and dielectric spectroscopy methods. The physical properties can be analyzed via the rheological, mechanical, and barrier performances.

4.2 Reciprocal Space Analysis

4.2.1 Small-Angle X-ray Scattering

The small-angle X-ray scattering (SAXS) method investigates “particles” which are composed of molecules grouped together in a random manner. It is a powerful technique for probing the distribution of NPs, as well as their shape, size, internal structures, crystal lamellar thickness, and surface per volume and/or mass.

4.2.1.1 Dispersion and Distribution of Nanoparticles in PNCs

In the case of PNCs, one of the biggest advantages of SAXS is that it probes materials with sub-nanometer resolution (1–100 nm) while analyzing a large sample size that covers a large number of NPs [2]. SAXS analysis is mainly applied for randomly oriented and statistically distributed particle systems. Hence, their 3D scattering pattern represents the orientational average of their structure. Only in the

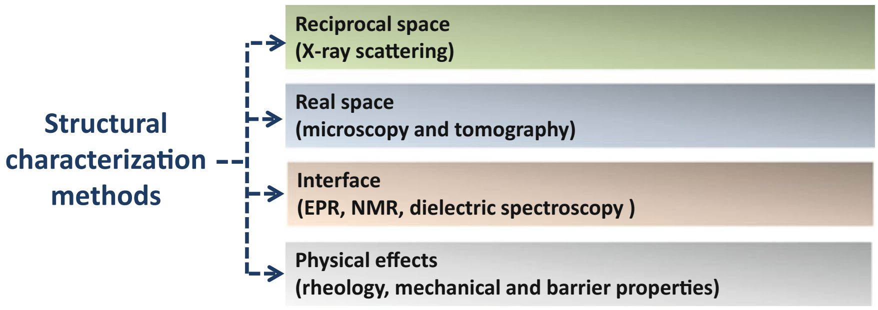

Fig. 4.1 The structural characterization methods used to analyse the polymer nanocomposites

case of three types of ideal symmetry (spherical, cylindrical, and lamellar structures with a centrosymmetric scattering length density distribution) there is no information loss due to orientational averaging [3]. This orientational averaging is radially symmetric and can therefore be reduced to the 1D angle-dependent scattering intensity function *I*(q) shown in (4.1).

$$I(q) = 4\pi \int_0^{\alpha} p(r) \frac{\sin qr}{qr} dr \tag{4.1}$$

where q is the scattering vector and can be related to the scattering angle (θ) and wavelength (λ) by (4.2).

$$q = \frac{4\pi}{\lambda} \sin\theta \tag{4.2}$$

The term $p(r)$ in (4.1) is the pair-distance distribution function of the electrons, which corresponds to the radial or spherical symmetric correlation function of electron density differences weighted by $4\pi r^2$. This term directly shows the probability of finding a pair of electron densities at a particular distance r. All information from the experimental curves in the small angle region is in reciprocal space as $q \propto 1/\lambda$. Therefore, it is difficult to yield direct information about the form and structure of the particles.

If we consider a composite particle consisting of sub-particles with a fixed orientation, the positioning of the centers of mass of the sub-particles can be written as $r_{1,}\ r_{2,} \ldots\ r_j \ldots\ r_N$. The scattered wave amplitudes from these sub-particles (with respect to each center) can be designated as F_1, F_2 , ..., F_j ..., F_N. The positions of the sub-particles are accounted for by an additional phase factor e^{-iqr_j}. Therefore, the total amplitude of the composite particle can be defined as follows:

$$F(q) = \sum_1^N F_j(q)\ .\ e^{-iqr_j} \tag{4.3}$$

In general, each amplitude will also have a phase; therefore, F_j can be defined as:

$$F_j = |F_j|\ .\ e^{i\varphi_j} \tag{4.4}$$

Then, intensity ($I(q)$) can be written as:

$$\begin{aligned} I(q) &= FF^* \\ &= \left\langle \sum_{j=k} \sum F_j F_k^*\ .e^{-iq(r_j - r_k)} \right\rangle + 2 \left\langle \sum_{j \neq k} \sum |F_j||F_k| \cos(qr_{jk} + q_k - q_j) \right\rangle \end{aligned} \tag{4.5}$$

The double sum contains N terms with $j = k$, where the phase factor consequently vanishes. The remaining term with $j \neq k$ represents the interference between the sub-particles according to the relative distance $r_{jk} = (r_j - r_k)$. Since each pair is counted twice with $r_{jk} = - r_{kj}$, only the real part is considered. Therefore, the intensity contribution with $j = k$ is considered the form factor and that with $j \neq k$ is considered the structure factor.

The real space transformation of the SAXS data (after desmearing) by inverse Fourier transformation (IFT) of the Fredholm integral equation (see (4.1)) can determine parameters such as $p(r)$, from which the form and structure factors can be evaluated. However, in this case, performing an IFT is impossible due to the termination effect of the q-scale and the influence of remaining background scattering, which can cause strong artificial oscillations ("Fourier ripples") in the $p(r)$ function and render the results useless [4, 5]. At small q-values, the measurement is limited by the unscattered primary beam and at large q-values by the progressive decrease in the signal-to-noise ratio. The scattered intensity is usually determined at discrete points. According to counting statistics, the standard deviation of each data point is equal to the square root of the number of pulses registered by the counter. The termination effect can be reduced by extrapolating the scattering curve. For example, the Guinier approximation [4, 5] can be used to extrapolate the scattering curve to a zero angle provided that the first data point is measured at a very small angle. The extrapolation to large angles can sometimes be performed using Porod's law. The termination effect can be minimized by the indirect Fourier transform method developed by Glatter [6, 7]. In most cases, researchers are interested in studying the structure of particles dispersed in solution; to avoid background scattering, the solvent is considered as a background, then the $I(q)$ of the solvent is subtracted from the $I(q)$ of the solution. In the case of polymer nanocomposites, in order to obtain information about the dispersed NPs, the response of the pure polymer should be taken as a background and subtracted from the scattering intensity of the nanocomposite. The generalized indirect Fourier transformation (GIFT) has the following advantages: single-step procedure; optimized general function system; weighted least square approximation; error propagation; minimization of the termination effect; and consideration of the physical smoothing condition given by the maximum intra-particle distance [5]. Therefore, for smoothing conditions it is necessary to estimate the upper limit of the largest particle dimension D_{max}. Therefore, if

$$r \geq D_{max}, \quad p(r) = 0 \tag{4.6}$$

In addition, a function system should be defined in the range $0 \leq r \leq D_{max}$ and a linear combination of these functions should provide $p(r)$. Therefore,

$$p_A(r) = \sum_{\upsilon=1}^{N} c_\upsilon \varphi_\upsilon(r) \tag{4.7}$$

where the suffix "*A*" denotes only that this $p(r)$ is approximated. N is the number of functions and should be chosen to sufficiently cover the range $0 \leq r \leq D_{max}$; c_υ contains the unknowns and can be determined by a weighted least square approximation of the experimental data. $\varphi v(r)$ are the cubic *B*-spline functions, which can be defined as multiple convolution products of a step function, representing curves with a minimum second derivative. Each individual spline function can be subjected to a Fourier transform (T_1), wavelength integral (T_2), slit-length integral (T_3), and slit-width integral (T_4). The intermediate result after Fourier transformation of all the splines represents the scattering intensity without the collimation effect corresponding to a distance distribution $\varphi v(r)$. Therefore, the intensity without the collimation effect $[\Psi_\upsilon(q)]$ can be expressed as:

$$\Psi_\upsilon(q) = T_1\varphi_\upsilon(r) \tag{4.8}$$

The smeared intensity (i.e., after adding the collimation effect) can be obtained after execution of T_2, T_3, and T_4 to give:

$$\chi_\upsilon(q) = T_4T_3T_2\Psi_\upsilon(q) = T_4T_3T_2T_1\varphi_\upsilon(r) \tag{4.9}$$

Hence, $\chi(q)$ represents the approximated scattering data from a particle with D_{max}. The next step is the stabilization of these coefficients. The stabilized least squares conditions are given below.

$$L + \lambda_L N_{c'} = \text{minimum} \tag{4.10}$$

$$L = \frac{\int_{q_1}^{q_2}\left[I_{\exp}(q) - \sum_{\upsilon=1}^{N} c_\upsilon\chi_\upsilon(q)\right]^2}{\sigma^2(q)}dq \tag{4.11}$$

$$N_{c'} = \sum_{\upsilon=1}^{N-1}(c_{\upsilon+1} - c_\upsilon)^2 \tag{4.12}$$

Here, q_1 and q_2 are the first and last data points, respectively, $I_{\exp}(q)$ is the experimental intensity, σ^2 is the estimated variance of the observed intensity, and λ_L is the stabilization parameter or Lagrange multiplier [5–7]. The optimum fit of the observed data points is given by:

$$I_A(q) = \sum_{\upsilon=1}^{N} c_\upsilon\chi_\upsilon(q) \tag{4.13}$$

$I_A(q)$ represents the approximated scattering curve, which should be similar to $I_{\exp}(q)$. Therefore, it can be concluded that the approximated distance distribution function $[p_A(r)]$ represents the $p(r)$ of the experimental curve.

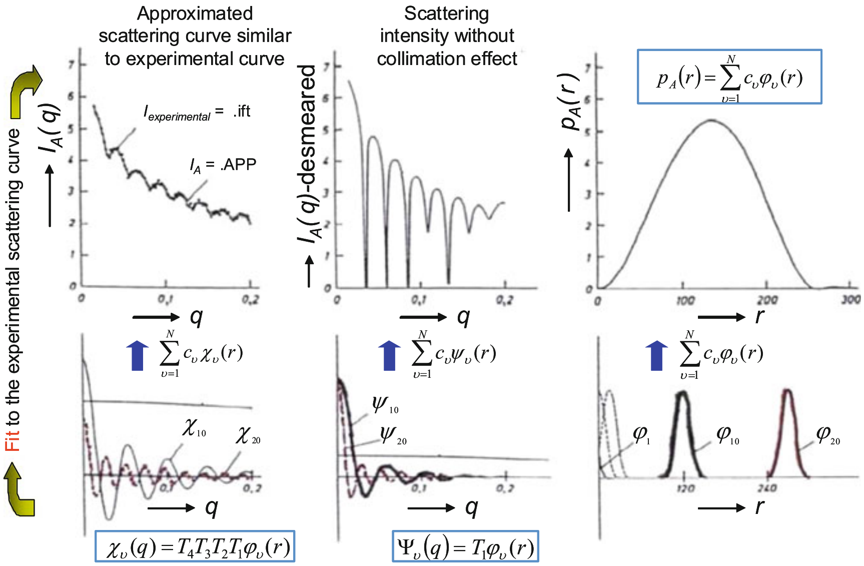

Smeared Fourier transformed splines (T_2, T_3, T_4 represents respectively wavelength, slit-length and slit-width integrals)

Fourier transformed splines (T_1 represents Fourier transformation)

Cubic *B*-spline functions

Fig. 4.2 The representative diagram of generalized indirect Fourier transformation (GIFT) method for spherical particle. Partially reproduced from [5] with permission

Figure 4.2 shows a representative diagram of the GIFT method for spherical particles, where $p(r)$ consists of N cubic B-spline functions and directly shows the probability of finding a pair of electron densities at a particular distance r [5]. Therefore, each spline function can be considered as the distance between a pair of dispersed NPs, for example stacked silicate layers. An advantage of the GIFT method is that the form and structure factors can be determined simultaneously from the measured scattering data with a correction for the instrumental broadening effect [8–10]. Therefore, to evaluate $p(r)$ from the scattering curve, one has to consider the values of N, D_{max}, and λ_L. If there is a difference between $I_A(q)$ and $I_{\exp}(q)$, then it is necessary to consider the effect of the structure factor.

D_{max} does need not to be a precise estimation of D. As a rough estimate, $D_{max} \leq (\pi/q_1)$, where q_1 is the lowest scattering angle. A theoretical limitation for the number of functions $N = N_{max}$ follows from the sampling theorem. A main concept of the indirect Fourier transformation technique is to start with a large number of coefficients to guarantee a sufficient representation of the distance distribution function. To approximate, $N_{max} \leq (q_2 \,.\, D_{max}/\pi)$, where q_2 is the maximum scattering angle. The stabilization parameter restricts the oscillation of the spline functions (i.e., oscillation of $p(r)$) and should be chosen so that the approximated scattering curve (determined on the basis of the $p(r)$) is similar to the experimental scattering curve. Only then can it be concluded that the $p(r)$ related to the approximated scattering curve is the same as that for the experimental scattering curve.

The structure factor is determined using the GIFT method with the modified Caillé theory for lamellar phases. There are two theories applicable to lamellar systems. Firstly, the paracrystalline theory, a general theory for disorder of the first and second kind was developed by Hosemann and Bagchi [11] and Guinier [12]. This was the first attempt to address the disorder in multilamellar arrays. The paracrystalline theory of the first kind assumes that there are stochastic distance fluctuations around the well-defined mean layer positions of equal separation; i.e., the long-range order is maintained. The paracrystalline theory of the second kind describes fluctuations of bilayer separations relative to the nearest neighbors of ideally flat bilayers. These fluctuations are not correlated and the long-range periodic order collapses [12]. However, the Caillé theory developed on the basis of the thermodynamic theory of DeGennes for smectic liquid crystals is preferable as it considers the bending of bilayers in addition to fluctuations in the mean spacing between them [13]. The modified Caillé theory proposed by Zhang et al. considers the finite size of the lamellar stack [14, 15]. This modification does not affect the quantitative results obtained by the original Caillé theory, but the modification is necessary to obtain better quantitative fits to the data and particularly for extracting the correct form factor, which could be used later to obtain an electron density profile.

As long as the bilayer is unilamellar, there exists a direct relationship between the electron density profile in the perpendicular direction to the midplane of the bilayer and the form factor. The lateral arrangement of multilamellar bilayers is represented by the structure factor and can be determined by either the paracrystalline or Caillé theory with a few parameters. It is necessary to assume either a form factor or a structure factor to evaluate the scattering data using the paracrystalline or modified Caillé theory. Frühwirth et al. [16] implemented the modified Caillé theory with GIFT to analyze stacked lamellar systems. This model is defined by three parameters: the number of coherently scattering bilayers (n); the repeat distance (d) of bilayer; and the Caillé parameter (η_1). According to the modified Caillé theory, the structure factor can be expressed as:

$$S(q) = n + \left\{ 2\sum_{m=1}^{n-1} (n-m)\cos(mqd)\exp\left[-\left(\frac{d}{2\pi}\right)^2 q^2\eta\gamma\right](\pi m)^{-(d/2\pi)^2 q^2 \eta_1} \right\} \tag{4.14}$$

where γ is Euler's constant (=0.5772). The parameter η_1 can be expressed as:

$$\eta_1 = \frac{q_1^2 k_B T}{8\pi (K_c B)^{1/2}} \tag{4.15}$$

where,

$$q = (2\pi/d) \tag{4.16}$$

K_c is the bending modulus and B is the bulk modulus for compression. Since the two moduli cannot be determined independently from the scattering data, one can consider η_1 as a measure of flexibility of the bilayers. According to the author, increasing the number of bilayers results in higher intensity and narrower peaks, and increasing the Caillé parameter leads to a faster decay of the peaks of higher order.

The electron density for the lamellae can be written as follows (assuming that the lamellae are homogeneous along the basal plane).

$$\rho(r) = \rho_0 \cdot \rho_t(x) \tag{4.17}$$

Here, ρ_0 is a constant and x is the normal distance from the central plane in the lamellae. Therefore, $\rho_t(x)$ represents the electron density along the thickness cross-section profile [5]. There are two ways to determine the electron density profile. In the conventional method, the scattering amplitude is determined from the scattering intensity by a simple square root operation. However, the main challenge is determining to correct sign (the so-called phase problem). The second method is estimating the electron density from the distance distribution function by a convolution square root technique. This method does not suffer from the phase problem. Hosemann and Bagchi [11] and Engel [12] showed that for the lamellar system, the convolution square root has a unique solution (except for a factor ± 1) if the function has a finite range of definition and the function is symmetrical [5]. Glatter used the convolution square root method in a different way. He deconvoluted the approximated electron density distribution in order to obtain the distance distribution function for highly symmetric systems (sphere, cylinder, or lamella). The electron density was approximated in its range of definition by a linear combination of a finite number of functions that have to be linearly independent in this range, expressed as follows:

$$\bar{\rho}(r) = \sum_{i=1}^{N} c_i \varphi_i(r) \tag{4.18}$$

where N is the number of functions, r is the normal distance from the center of symmetry, $\varphi_i(r)$ is the equidistant step function (cubic B-spline of zero order) with a width ΔR allowing analytical integration of the overlap integrals, and c_i is the height of the step functions. Equation (4.18) corresponds to a nonlinear distance distribution function (see (4.19)), which can be solved in an interactive stabilized manner to describe the $p(r)$ function obtained from IFT/GIFT methods [17–19].

$$\bar{p}(r) = \sum_{i=1}^{N} V_{ii}(r) c_i^2 + \sum_{i > k} V_{ik}(r) c_i c_k \tag{4.19}$$

If there is some deviation from high symmetry, which is known as the polydispersity of a sample, then the *p*(*r*) determined by the deconvolution (DECON) method (performed using DECON software) will be slightly different than the value determined from GIFT. By estimating the amount of polydispersity, a good match between the *p*(*r*) values determined by GIFT and DECON can be achieved. Therefore, the electron density distribution derived from DECON should represent the experimental scattering curve.

Although XRD is used widely to analyze the dispersion of nanoclays in polymer nanocomposites, SAXS is beneficial for probing the dispersion characteristics of highly delaminated structures [1, 20–23]. Additionally, as discussed above, GIFT allows detailed investigation on the inter-particle correlation function and internal structure from the electron density distribution [24, 25]. SAXS analysis has demonstrated that the filler loading plays a vital role in controlling the network structure of dispersed silicate layers in a polymer matrix [24]. The current authors have extensively exploited this method for clay-containing poly[(butylene succinate)-co adipate] (PBSA) nanocomposites and determined the percolation threshold concentration of the nanoclay [24]. The *p*(*r*) values of various nanocomposites obtained from GIFT analysis are shown in Fig. 4.3 [24]. The regions with opposite signs of different electron density give negative contributions to *p*(*r*). The *r*-value at

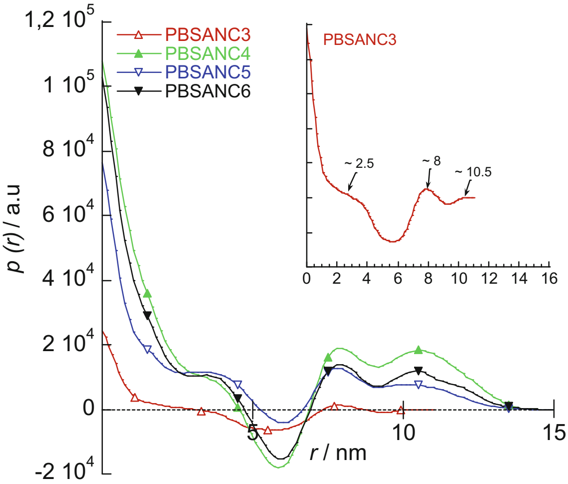

Fig. 4.3 The pair-distance-distribution function, *p*(*r*) for nanocomposites showing the probability of finding neighboring particles in systems with increase in clay concentration. PBSA nanocomposites (PBSANCs) with four different C30B loadings of 3, 4, 5, and 6 wt%, were abbreviated as PBSANC3, PBSANC4, PBSANC5, and PBSANC6, respectively. Reproduced with permission from [24]. Copyright 2010, Elsevier Science Ltd

which $p(r)$ drops to zero indicates the largest single particle dimension. As evidenced from the figure, the number of correlation maxima (peaks) increases with an increase in nanoclay loading. These correlation maximums represent the average radial distance to the next neighboring domain, commonly known as long spacing. When the neighbors overlap, the peaks do not possess a tail; rather, the curve shows a maxima and minima.

The electron density profiles obtained from the $p(r)$ values (see Fig. 4.4) showed that the nanocomposites had a core–shell particle structure [24]. When the clay platelets started delaminating in the nanocomposites, these core-shell structures start to grow with the previously peeled nanoclay layers as a shell. PBSANC3 had a core thickness of approximately 6 nm and a shell layer thickness of 2.6 nm. In the case of PBSANC4, the core thickness decreased and the total shell thickness for the two shells increased dramatically. There was no remarkable subsequent change in core thickness or total shell thickness for either PBSANC5 or PBSANC6. Therefore, the percolation threshold value of C30B loading in the case of C30B-containing PBSANCs was 5 wt%.

The SAXS spectra and electron density profile obtained from the *in situ* temperature-assisted SAXS can elucidate the molecular dynamics mechanisms of nanocomposite formation [26]. It was shown that the absorbed moisture of fumed silica had a plasticizing effect on the polycarbonate (PC) matrix. Plasticization advanced the segmental movement of PC chains in the PC/fumed silica composite above 150 °C.

The number of aggregated particles (N_{agg}) dispersed in a polymer matrix can be determined according to (4.20) [27]:

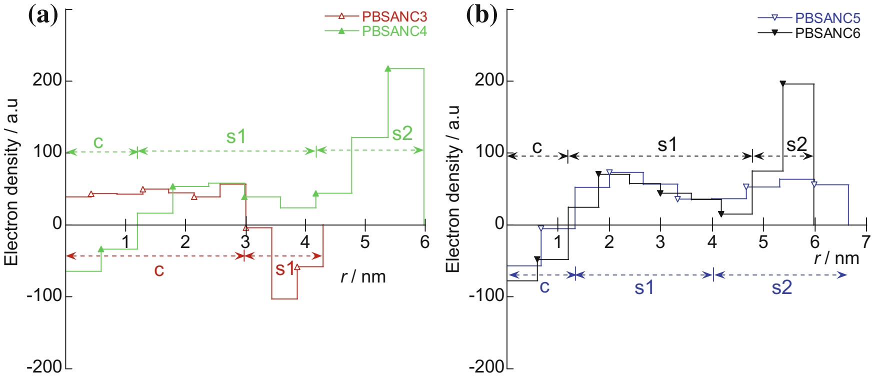

Fig. 4.4 Electron density profile of the model nanocomposites: **a** for PBSANC3 and PBSANC4 and **b** for PBSANC5 and PBSANC6. PBSA nanocomposites (PBSANCs) with four different C30B loadings of 3, 4, 5, and 6 wt%, were correspondingly abbreviated as PBSANC3, PBSANC4, PBSANC5, and PBSANC6, respectively. Here the core is denoted by 'c', inner shell by 's1' and outer shell by 's2'. Reproduced with permission from [24]. Copyright 2010, Elsevier Science Ltd

$$N_{\mathrm{agg}} = \left(\frac{2\pi}{q^*}\right)^3 \left(\frac{\varphi}{V}\right) \tag{4.20}$$

where q^*, φ, and V are the scattering peak position, volume fraction, and volume of the particle, respectively.

4.2.1.2 Orientation of Dispersed Nanoparticles in Polymer Nanocomposites

X-ray scattering has been extensively used to estimate the gallery spacing of nanoclay platelets dispersed in polymer nanocomposites. The disappearance of a discrete peak is attributed to exfoliation. However, such interpretation might be misleading sometimes. The preferred in-plane orientation of platelet-type nanoclays in the nanocomposite can drastically reduce the scattering intensity, as shown in the Fig. 4.5 [23, 28]. The schematic diagrams (Fig. 4.5a, b) describe the interaction of

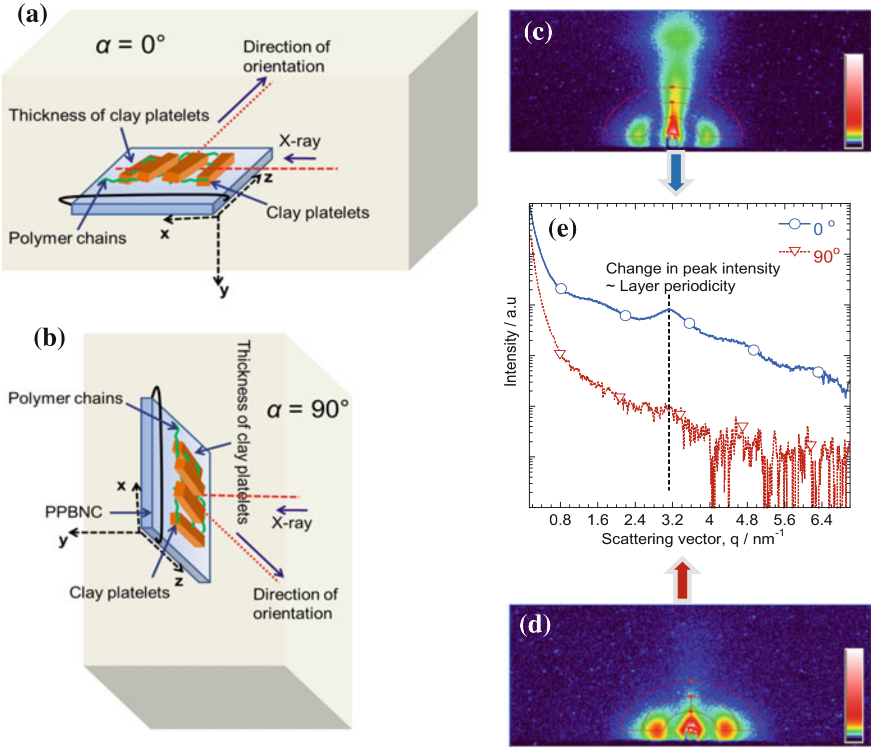

Fig. 4.5 **a**, **b** The schematic diagrams showing the interaction of X-ray with the polymer chains and the nanoclays at different planes; **c**, **d** corresponding 2D-scattering patterns; and **e** the normalized scattering intensity as a function of *q*

X-rays with polymer chains and nanoclays in different planes. The 2D-scattering patterns (Fig. 4.5c, d) and the normalized scattering intensity as a function of q (Fig. 4.5e) show that the intensity and appearance/disappearance of a peak depends on the angle of interaction between the X-ray and particle.

In a densely packed system of particles, the positional ordering can develop a preferential orientation, especially when particles are not spherical. The degree of orientation can be easily detected from 2D SAXS patterns. Usually, an arc-profile is used to determine the orientation of crystals in a certain basal plane. A point on the azimuthal scan can be presented by a unit vector, u, such that $u_1 = \cos\beta$ and $u_2 = \sin\beta$; where β is the azimuthal angle. The anisotropy in the X-ray scattering pattern can be obtained from the weighted average of the second moment tensor of u following:

$$\langle uu \rangle = \begin{bmatrix} \langle u_1u_1 \rangle \langle u_1u_2 \rangle \\ \langle u_1u_2 \rangle \langle u_2u_2 \rangle \end{bmatrix} = \begin{bmatrix} \left\langle \cos^2\beta \right\rangle \langle \sin\beta\cos\beta \rangle \\ \langle \sin\beta\cos\beta \rangle \left\langle \sin^2\beta \right\rangle \end{bmatrix} \tag{4.21}$$

Here, $\langle \cdots \rangle$ represents an average weighted by the azimuthal intensity distribution and e.g., $\left\langle \cos^2\beta \right\rangle$ can be expressed as,

$$\left\langle \cos^2\beta \right\rangle = \frac{\int_0^{2\pi} \cos^2\beta I(\beta)d\beta}{\int_0^{2\pi} I(\beta)d\beta} \tag{4.22}$$

The difference in eigenvalues $(\lambda_1 - \lambda_2)$ of $\langle uu \rangle$ gives a measure of the anisotropy factor and can be expressed as:

$$\lambda_1 - \lambda_2 = \sqrt{(\langle u_1u_1 - u_2u_2 \rangle)^2 + 4\langle u_1u_2 \rangle^2} \tag{4.23}$$

The degree of anisotropy determined by the software program ‘tdoa’ is $(\lambda_1 - \lambda_2)$ in percent. The mean orientation angle or the average domain orientation angle can be expressed as:

$$\bar{\chi} = \frac{1}{2}\tan^{-1}\left(\frac{2\langle u_1u_2 \rangle}{\langle u_1u_1 \rangle - \langle u_2u_2 \rangle}\right) \tag{4.24}$$

The sample can be oriented either due to shear and stretching processes during polymer processing or upon experiencing thermal and mechanical treatments [28–30]. Conventionally, point collimation with or without a vario-stage (that enables tilting, rotation, and scanning at different positions) is used to collect the scattering spectrum for such analysis. At an instance after tensile stretching, the orientations of pure polymer (PBSA) and nanocomposite (PBSANC3) were determined by tilting, rotating, and scanning the specimens with respect to the incident X-ray beam [28]. It was shown that the dispersed clay platelets were oriented along the z-axis, i.e., the direction of elongation during tensile testing. The second observation was that the thicknesses of the clay layers were in the xy- and yz-planes. The surface of the clay platelets were in the xz-plane (see Fig. 4.5a, b). In addition to determining particle dispersion and distribution, SAXS instruments fitted with Linkam shearing or stretching devices can analyze the time dependent structural changes during stress relaxation and hysteresis [31]. The authors observed that the nanoclay orients almost instantaneously, while the polymer chains become elongated in the stretching direction, followed by delamination off the polymer chains that were adsorbed on the nanoclays.

Processing conditions, such as variations in the feeding rate during extrusion, can affect the orientation of the nanoclay platelets in the polymer nanocomposite [32]. Figure 4.6 shows that increasing the feed rate resulted in a random distribution of nanoclay in the nanocomposite, while a slower feed rate allowed orientation of the nanoclay platelets to occur. The shearing device coupled with the SAXS system elucidated changes in the orientation angle and anisotropy factor as a function of shear rate [33]. In addition, compression can also introduce anisotropy, e.g., in the blend composite of polypropylene (PP)/ethylene-propylene-diene terpolymer rubber (EPDM)/Cloisite® 15A (C15A) [34].

4.2.1.3 Lamellar Crystal Thickness

SAXS can also be employed to estimate the lamellar crystal thickness from the first-order long period. To achieve this, the first- and second-order reflections are

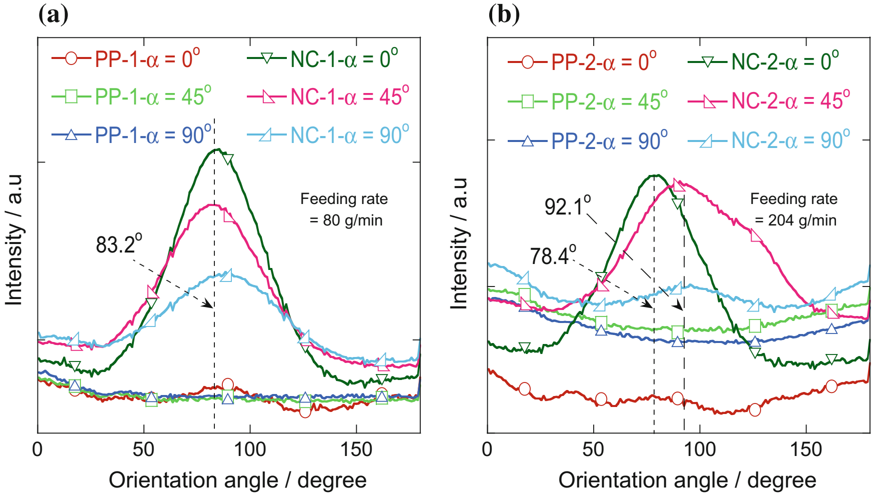

Fig. 4.6 Change in orientation of clay platelets with the feeding rate **a** NC-1 and **b** NC-2. Feed rate used for NC1 and NC2 were 80 and 204 g/min, respectively

separated by fitting the scattering profile with the product of Gaussian and Lorentzian functions [35]. Then, the first- (l_1) and second (l_2)-order long periods can be estimated using Bragg's law. The lamellar crystal thickness (l_c) can then be estimated as follows:

$$l_c = \varphi l_1 \tag{4.25}$$

where, φ is the crystallinity of the material at a particular condition. As an estimation, the chain dimension in the melt is the radius of gyration (R_g), the condition for crystallization without disentanglement is:

$$l_c \le R_g \tag{4.26}$$

Fu et al. [36] assumed that if the crystal is smaller than the chain dimension (i.e., satisfying (4.26)), disentanglement may not be required for crystallization from the melt state. The entanglements can be shifted toward the amorphous region, which eventually can form stereo-defects as noncrystallizable entities. However, if $l_c > R_g$, crystallization occurs via disentanglement of polymer chains. For Gaussian chains, R_g can be estimated from (4.27) [35]:

$$R_g^2 = \frac{R_0^2}{6} \tag{4.27}$$

where, R_0 is the mean squared end-to-end distance and can be calculated using the characteristic ratio C_∞, sum of the square of the length of backbone bonds in one monomer unit (a_b^2), and degree of polymerization (N), as shown below [35]:

$$R_0^2 = C_\infty a_b^2 N \tag{4.28}$$

The long period (and hence, lamellar thickness) as a function of nanoclay concentration in a polyamide 6(PA6)/NanomerI.30TC composite showed that the crystalline morphology of PA6 changed dramatically in the presence of the nanoclay [20].

4.2.1.4 Particle Dimension and Specific Surface Area

R_g is determined from the Guinier equation below:

$$I(q) = (\Delta\rho)^2 V^2 \exp\left(-\frac{q^2 R_g^2}{3}\right) \tag{4.29}$$

R_g does not contain any information about the shape and internal structure of the particle [4]. However, by knowing R_g and the form factor of scattering [$P(q)$], it is possible to estimate the average radius of the particle. The value of [$P(q)$] can be approximated by a Gaussian curve at small angles, where the curvature of the Gaussian depends on the overall size of the particle [4]. In the case of spherical particles,

$$P(q) \approx a_0 \exp\left(\frac{-R_g^2}{3} q^2\right) \tag{4.30}$$

The parameter a_0 can be extrapolated to zero angle intensity and $a_0 = 1$ to the zero angle position. Since the intensity is directly proportional to $P(q)$,

$$\ln[\Delta I(q)] = \ln[a_0] - \frac{R_g^2}{3} q^2 \tag{4.31}$$

Therefore, R_g and a_0 can be determined from $\ln[\Delta I(q_0)]$ versus q^2 curves (a Guinier plot). Similarly, the radius of gyration of the cross-section of cylindrical particles (R_C) and the thickness radius of gyration of lamellar particles (R_T) can be determined from (4.31) and (4.32), respectively [4].

$$qP(q) \approx a_0 \exp\left(\frac{-R_C^2}{2} q^2\right) \tag{4.32}$$

$$q^2 P(q) \approx a_0 \exp\left(-R_T^2 q^2\right) \tag{4.33}$$

Multiplying $P(q)$ by q (see 4.31) eliminates the contribution of the axial dimension (assumed to be infinitely long). Similar logic can be applied for the lamellar structures; hence, $P(q)$ is multiplied by q^2 in 4.32. Initial slopes of 0, −1, and −2 indicate globular, cylindrical, and lamellar-shaped particles, respectively (see the log [$P(q)$] vs. log q plot shown in Fig. 4.7). The average radius for spherical and cylindrical particles and the half thickness for a homogeneous plate can be determined from (4.34) to (4.36).

$$Radius\ of\ spherical\ particle = \sqrt{\frac{5}{3}} R_g \tag{4.34}$$

$$Radius\ of\ cylindrical\ particle = \sqrt{2} R_C \tag{4.35}$$

$$Half\ thickness\ of\ platelets = \sqrt{3} R_T \tag{4.36}$$

The specific surface area and interfacial area can also be estimated using SAXS [37]. The intensity of the tail region of the scattering pattern is approximated by Porod's law:

$$\lim_{q\to\infty}\left[I(q)q^3\right] = \frac{(\Delta\rho)^2 S}{16\pi^2} \tag{4.37}$$

Here, S is the surface area of the particle and can be determined from (4.37) by knowing the absolute intensity. Equation (4.37) is independent of the dimension, shape, and porosity of the particle and valid for a concentrated system where interfaces between the particles have little effect on the tail of the SAXS spectrum. However, measurement of the absolute intensity in order to determine S can be avoided by considering the invariant Q:

$$Q = \int_0^\infty 2\pi q I(q) dq = (\Delta\rho)^2 V \tag{4.38}$$

Therefore, (4.37) reduces to

$$\lim_{q\to\infty}\left[I(q)q^3\right] \cdot \frac{16\pi^2}{Q} = \frac{S}{V} \tag{4.39}$$

The correlation between S and R_g for nanoclay-containing composites of natural rubber (NR) and styrene butadiene rubber (SBR) composites is presented in Fig. 4.8 [37]. As evidenced from the figure, the interfacial area decreases with increasing size of the agglomerated/stacked nanoclays.

SAXS can also be employed to determine the surface per mass (S_M) according to (4.40) and (4.41).

$$S_M = 1000\pi \frac{\varphi(1-\varphi)}{d}\frac{K}{Q} \quad \text{(for desmeared scattering data)} \tag{4.40}$$

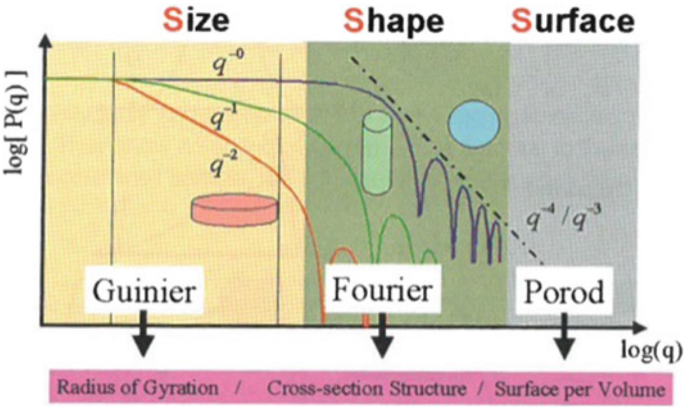

Fig. 4.7 The information domain of a particle form factor. Reproduced with permission from [4]. Copyright 2006, Anton Par GmbH

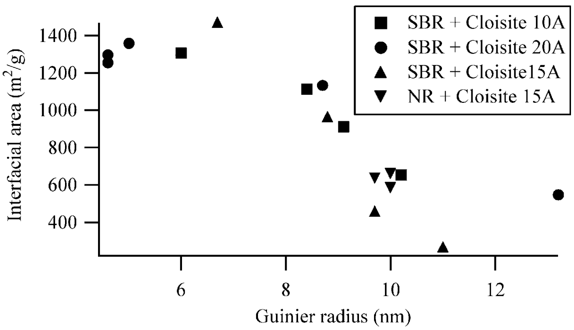

Fig. 4.8 Trend of the matrix/clay interfacial area as a function of the radius of gyration of clay particles. Reproduced with permission from [37]. Copyright 2012, the American Chemical Society

$$S_M = 4000\pi \frac{\varphi(1-\varphi)}{d}\frac{K}{Q} \quad \text{(for smeared scattering data)} \tag{4.41}$$

Here, φ, d, and K represent the volume fraction, density, and intercept of the Porod plot, respectively. The invariant, Q can be expressed as the sum of Q_1 (Guinier extrapolation), Q_2 (experimental), and Q_3 (Porod extrapolation). Furthermore, correlation between the interfacial surface area and the moduli (see Fig. 4.9) shows that the stiffness/tensile modulus of the composite increased with increasing total interfacial area [37].

4.2.2 X-ray Diffraction

In principle, X-ray diffraction (XRD) is fundamentally similar to the SAXS; both techniques are used to extract structural information. However, SAXS provides

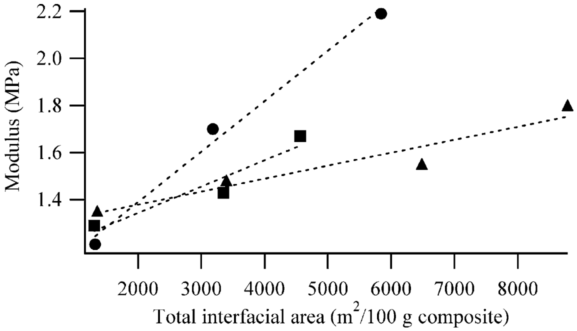

Fig. 4.9 Elastic modulus as a function of interfacial area, circles represents the NR-based composites, square represent SBR10 composite series and triangles indicate SBR20 composite series. The lines were drawn to show the trend. Reproduced with permission from [37]. Copyright 2012, the American Chemical Society

information related to the particle as a whole, while XRD probes atomic arrangements (crystal structures) inside the particle. Therefore, combining both SAXS and XRD data is very powerful for analyzing multi-component systems such as polymer composites. XRD is mainly used to determine the atomic structure of a crystal. The incident X-ray interacts with the atoms and is diffracted in specific directions. Understanding the crystal structure is important for e.g., identifying compounds, ores, and polymorphs, and analyzing material fatigue; it is important to note that the integral intensity depends on the volume fraction of the phases, crystal structure (structure factor), lattice vibration (temperature factor), composition and ordering in the solid solution, aggregate structure (microabsorption), orientation distribution (texture factor), and lattice defects [38]. Similarly, the peak position depends on the composition in the solid solution, thermal expansion, and internal stresses (kind I) [38]. The shape of the peak (broadening) depends on the internal stresses (kind II and III), particle size, stacking faults, and dislocation substructure [38].

In PNC research, XRD is an important tool for probing the dispersion of the NPs in the polymer matrix. XRD is also used to determine the crystal lattice and size of the polymer crystal. Properties of the polymer, such as the transparency, and the mechanical, thermal, and barrier properties can be directly correlated with the shape and size of the crystals. Smaller crystallite sizes generally have better transparency and mechanical performance, while larger spherulites (crystals) sometimes can impede the permeation of gas molecules [39].

4.2.2.1 Dispersion Characteristics

XRD has been employed to investigate the dispersion of different types of NPs (e.g., nanoclays, graphene, and metal oxide particles) dispersed in various polymer matrices [40–44]. The *d*-spacing between the two crystal planes is determined by Bragg's law:

$$n\lambda = 2d\sin\theta \tag{4.42}$$

where, n, λ, d, and θ represent a positive integer, wavelength of the incident X-ray, *d*-spacing of the crystal, and the scattering angle, respectively.

Figure 4.10 shows XRD patterns of nanoclay and PP nanocomposites in the small-angle region [32]. In both nanocomposites (NC-1, PNC processed at a feeding rate of 80 g/min and NC-2, PNC processed at a feeding rate of 204 g/min), the ratio of PP:PP-g-MA(maleic anhydride grafted PP):silicate content of clay was kept at 97:9:3. Two different feeding rates (80 and 204 g/min) were used during the dilution of the PP-g-MA/Cloisite® C20A (C20A) master batch in PP. The figure shows a characteristic peak of the C20A nanoclay at 3.6°, corresponding to a $d_{(001)}$-spacing of 2.45 nm. In NC1 and NC2, this peak shifted towards smaller angles, appearing at 2.5° and 2.7°, respectively (corresponding to $d_{(001)}$-spacings of 3.61 nm and 3.29 nm, respectively). Such an increase in the *d*-spacing indicates that the polymer chains were intercalated in the clay gallery. Another interesting

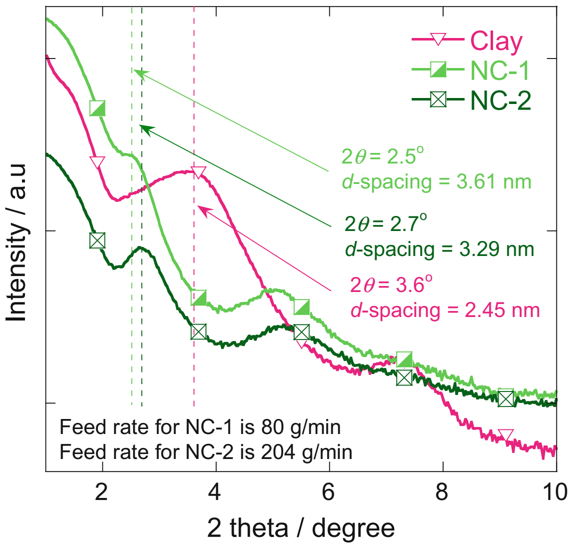

Fig. 4.10 X-ray diffraction patterns of compression molded polypropylene nanocomposites in the small angle region

observation is that the characteristic XRD peak was weaker for NC1 than for NC2, even though they contain almost the same amount of silicate. Hence, parallel stacking of the dispersed clay was lower in NC1 than in NC2.

In addition to the dispersion of nanoclays, XRD can provide information about the interaction of the nanofiller with the polymer matrix. Shanthala et al. [45] observed an amorphous halo from polypyrrole (PPy). However, many small crystal peaks appeared for a PPy/copper zinc iron oxide nanocomposite due to interaction of the NPs with the polymer via chemical bonding or interaction with macromolecular chains of the matrix. Furthermore, Zhu et al. [41] showed that when graphene oxide (GO) nanosheets absorb carrageenan (Car) macromolecules through hydrogen-bond interactions, the interlayer spacings between GO nanosheets increased.

4.2.2.2 Analysis of Crystal Phase

Different crystal structures of the same material are important for many applications. For example, the presence of both anatase and rutile phases of TiO_2 in polyaniline (PANI) nanocomposites plays an important role in improving the photocatalytic activity [46]. The synergistic effect of both anatase and rutile phases inhibit the recombination of the electron-hole pair. Identification of crystal structure is also important to predict the mechanical properties. For example, in the presence of β-crystals, isotactic PP exhibits improved elongation at break, and higher toughness and impact strength, while the α-polymorph shows increased stiffness

[47, 48]. Therefore, a combination of α- and β-crystals can provide optimum toughness and stiffness.

In the case where all samples have the same surface roughness and thickness, the optical transparency depends on the crystallinity. When the overall crystallinity is similar, the amount of -phase could be the controlling factor. De Santis and Pantani [49] demonstrated the dependence of the crystallinity on the cooling rate and the number of recycling steps. It is interesting to note that while the α-phase crystallinity decreased with increasing cooling rate, the mesomorphic phase fraction increased with the number of recycling steps. Moreover, the authors correlated the birefringence and opacity of the PP samples before and after recycling steps with the amount of α-phase present in the samples. Birefringence is an optical phenomenon where polymer exhibits different refractive indices for light with plane polarization in two perpendicular directions (ordinary and extraordinary rays). According to the reported results, the birefringence and hence, opacity of the polymer, increased with increasing α-phase crystallinity. Such results are important for product development. The phase and its degree of crystallinity also play important roles in the gas barrier performance of polymers [39]. The degree of crystallinity (X_c) can be determined from the intensity of the crystalline peaks (I_c) and the amorphous region (I_a).

$$X_c = [I_c/(I_c + I_a)] \, . \, 100 \tag{4.43}$$

Malas et al. [50] established a correlation between the increase in the glass transition temperature and degree of crystallinity, and the dielectric strength of the interfacial polarization for a polyethylene oxide and reduced graphene oxide system. The authors found that the strength of the interfacial entrapment of charges during dielectric spectroscopy is related to reduced mobility of the polymer chains.

Another important crystal parameter influencing the properties of polymeric composites is the crystallite size, L, which can be estimated by the well-known Scherrer equation:

$$L = \frac{K\lambda}{\beta \cos\theta} \tag{4.44}$$

Here, K, λ, β, and θ are the Scherrer constant (≈1), wavelength of the incident X-ray beam, full-width-at-half-maximum of the peak, and the scattering angle, respectively. Subsequently, the number of crystallites per unit area (C) in the film can be estimated as follows [51].

$$C = \frac{t/L^3}{unit\,area} \tag{4.45}$$

Various X-ray diffraction analysis methods (such as pole figure construction and Fourier transform peak shape deconvolution) can be employed to quantify texture changes, and the relative degree of crystallinity and lattice order. The texture coefficient (TC) of each (*hkl*) plane is determined from the XRD spectrum using (4.46) [52].

$$\mathrm{TC}_{(hkl)} = \frac{I_{(hkl)}}{I_{0(hkl)}}\left[\frac{1}{N}\sum_{i=1}^{N}\frac{I_{(h_ik_il_i)}}{I_{0(h_ik_il_i)}}\right]^{-1} \tag{4.46}$$

where I $(h_ik_il_i)$ is the intensity of the $(h_ik_il_i)$ diffraction peak of the sample under investigation; I_0 $(h_ik_il_i)$ is the intensity of the $(h_ik_il_i)$ plane of a completely random sample taken from a powder diffraction file (PDF) card; and N is the number of diffractions considered in the analysis. For randomly oriented crystals, $\mathrm{TC}_{(hkl)} = 1$ [53]. Higher values indicate more grains oriented in a given (*hkl*) direction.

4.3 Analysis in Real Space

4.3.1 Electron Microscopy

In electron microscopy (EM), an electron beam is used for imaging, where the interaction between the electron beam and the sample produces various scattering signals. Different electron microscopy techniques, such as transmission EM (TEM), scanning TEM (STEM), and focused ion beam scanning EM (FIB-SEM) allow qualitative analysis of the internal structure via direct visualization. Some microscopy techniques require sample preparation involving either a microtome or milling by ion-beams. In the case of SEM, two types of signals are usually detected; secondary electrons and backscattered electrons. The secondary electrons originate from the surface, or close to surface, and are due to inelastic interaction between the primary electron beam and atoms in the samples. These are beneficial for imaging the surface topography. In contrast, backscattered electrons originate due to elastic collisions of electron beam with the atoms. As the probability of elastic collision increases with increasing size of the atom, larger (heavier) atoms produce stronger scattering signals than smaller (lighter) atoms. Hence, the backscatter signal is directly proportional to the atomic number. Therefore, backscattered signals are useful for detecting different phases or compositions in the sample.

The dispersion characteristics of nanoclays in PBSANC3 after tensile stretching are shown in Fig. 4.11 [54]. Further image analysis by energy dispersive spectroscopy (EDS) confirmed that the dark features were nanoclay platelets which were well-oriented in the direction of the applied tensile strain. To gain a deeper understanding of the degree of dispersion of the nanoclays in the polymer matrix, EM images can be further analyzed by image processing. STEM images and the image analysis process are depicted in Fig. 4.12, showing that the nanoclay loading plays a vital role in controlling the network structure [24]. These results also showed that 5 wt% nanoclay was the percolation threshold for forming a strongly flocculated structure of dispersed silicate layers. The authors also reported that the

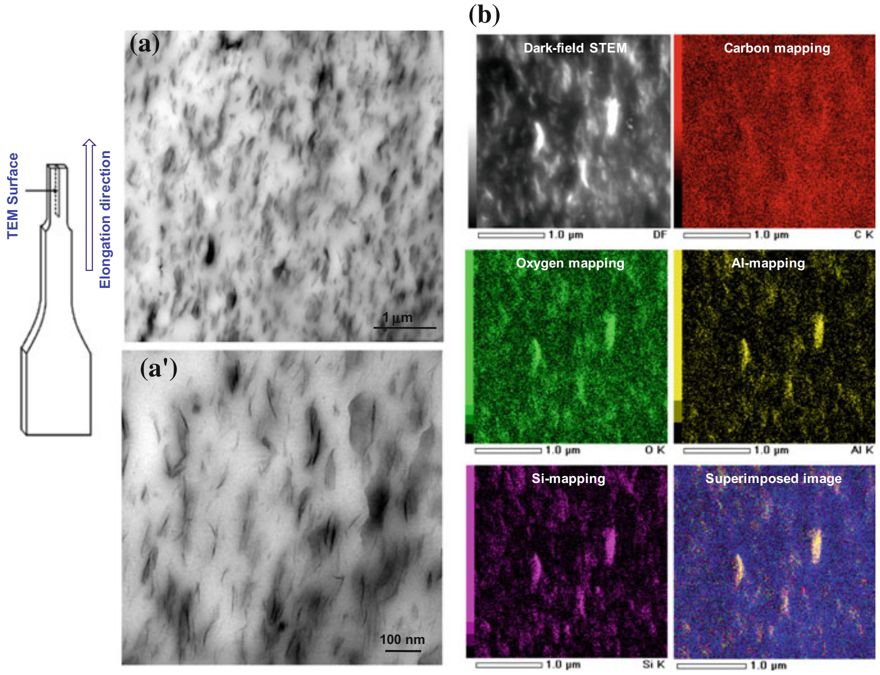

Fig. 4.11 **a**, **a′** Bright-field TEM image of nanocomposite sample after tensile test and **b** X-ray mapping of various elements in scanning transmission electron microscopy mode. This result shows silicate layers are oriented towards the direction of applied strain. Reproduced with permission from [54]. Copyright 2010, Elsevier Science Ltd

dispersion characteristics of nanoclays influence the melt-flow behaviors of nanocomposites.

SEM is commonly used to investigate the properties of e.g., fracture surfaces and the morphology of polymer blends. SEM equipped with EDS provides elemental information of the nanoparticle dispersed in the PNCs. Depending on the contrast of the electron density; SEM can also be used to determine the thickness of individual layers present in the multilayered structure.

3D-tomography using a FIB-SEM cross-beam system can be used to analyze the orientation of NPs (e.g., nanoclays) dispersed in a polymer matrix. Such analysis is complementary to SAXS analysis. The process involves cutting 2D-slices through a selected volume by ion-beam milling, then imaging the cross-section using high-resolution SEM (HR-SEM). The 2D-images are then aligned by cross correlation of reference markers, and finally, computer reconstruction of 2D-images enables the generation of a 3D-morphology of the dispersed nanoclays in the polymer matrix. Around 100 images from more than 300 x–y cross-sections are used for 3D-reconstructions. 3D-reconstructed images at different planes of PBSANC3 samples (after tensile tests) are shown in Fig. 4.13 [28]. The first clear observation is that the dispersed nanoclay platelets are oriented along the z-axis,

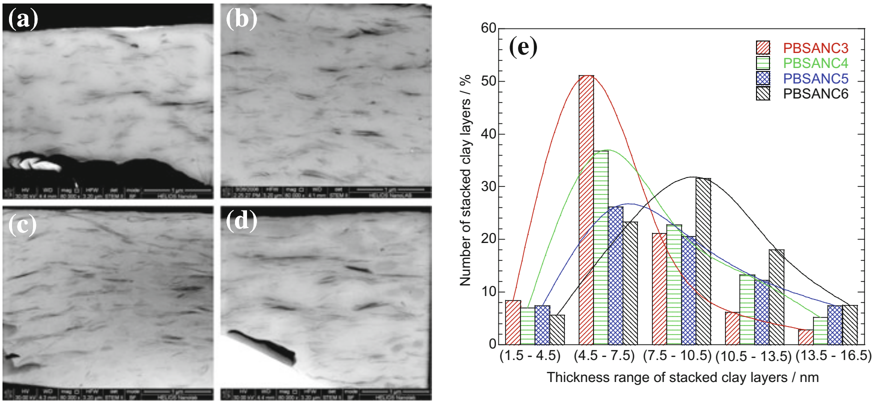

Fig. 4.12 The bright-field scanning transmission electron microscopy (STEM) images of four different nanocomposite systems, in which black entities represent the dispersed silicate layers: **a** PBSANC3 (containing 3 wt% C30B), **b** PBSANC4 (containing 4 wt% C30B), **c** PBSANC5 (containing 5 wt% C30B), and **d** PBSANC6 (containing 6 wt% C30B). **e** The number of stacked silicate layers (in %) for the different nanocomposites is plotted against the thickness of the stacked silicate layers (in nm) determined on the basis of the STEM images. Image J software was used to analyze STEM images (for each sample 280 tactoids were considered). Reproduced with permission from [24]. Copyright 2010, Elsevier Science Ltd

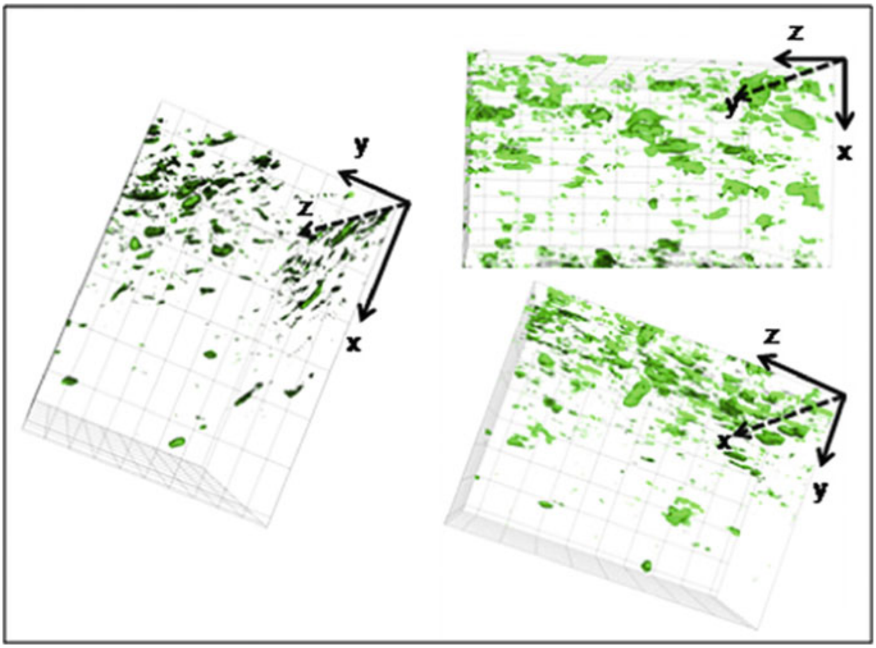

Fig. 4.13 The 3D-constructed images at different planes of the PBSANC sample by focused ion beam scanning electron microscope

i.e., the direction of elongation during the tensile test. The second observation is that the thicknesses of the clay layers are in the xy- and yz-planes. The surface of the clay platelets is in the xz-plane.

3D distributions of nanoclay platelets in polymer blends have also been visualized using electron tomography (or 3D TEM) [55]. Using a Gatan Ultrascan camera (resolution of 2–5 nm), 2D projection images with tilt angles ranging from −45° to +45° were automatically acquired in 2° increments at 200 kV. Using TEMography™ software, the tilted images were aligned to a common origin and subsequently reconstructed using a simultaneous iterative reconstruction technique. 3D distributions of nanoclay platelets in the blends are shown in Fig. 4.14a–d. The dark features represent the dispersed nanoclay particles in the blend composites. Figure 4.14a′–d′ and a″–d″ show 3D projections of a selected region of the 3D TEM images (refer to Fig. 4.14a–d). The blue markers in Fig. 4.14a′–d′ and a″–d″ represent the dispersed nanoclay particles and the silver, gold, and yellow colors in the background represent nylon 6 (N6), ethyl vinyl alcohol (EVOH), and the N6/EVOH blend, respectively. The images of various samples clearly show that the intercalated silicate layers of the nanoclay were preferentially oriented. It was clear that the nanoclay was located only in the interphase region in N6/EVOH/MB and formed core–shell particles. Such localization of intercalated silicate layers could suppress coalescence and stabilize the blend morphology. However, the intercalated silicate layers were well dispersed in the blend matrix of the N6/EVOH/OMMT composite; it was difficult to differentiate between the two phases.

4.3.2 Fourier Transformed Infrared Spectroscopy

FTIR spectroscopy is a powerful and versatile tool for analyzing the structure of multicomponent systems such as polymer blends, nanocomposites, and blend nanocomposites at the molecular level. The presence of additives, contaminants, degradation by-products, and chemical bonding at the interface of multi-layered polymer systems, polymer blends and/or the polymer–nanoparticle interface can be resolved using this technique [56]. The IR measurements in transmission mode require optically thin samples, preferably with thickness in the micron range. Various analysis modes can be used. A line scan across the cross-section can provide detailed information regarding the composition of the layers of multi-layered structure or laminates. This technique can also be employed to probe the absorption topography of polymer nanocomposites, as shown in Fig. 4.15 [57]. A noticeable change in the topography can be observed after changing the nanoclays (C20A and C30B) in the PBSA nanocomposites. The different nanoclays had different dispersion and interactions with the PBSA matrix, resulting in different topographical features.

In another study, FTIR spectra were extracted at different positions of absorbance images, as shown in Fig. 4.16. The absorption topography of PA and a PA PNC are shown in images (a) and (a′). False color absorbance images are shown

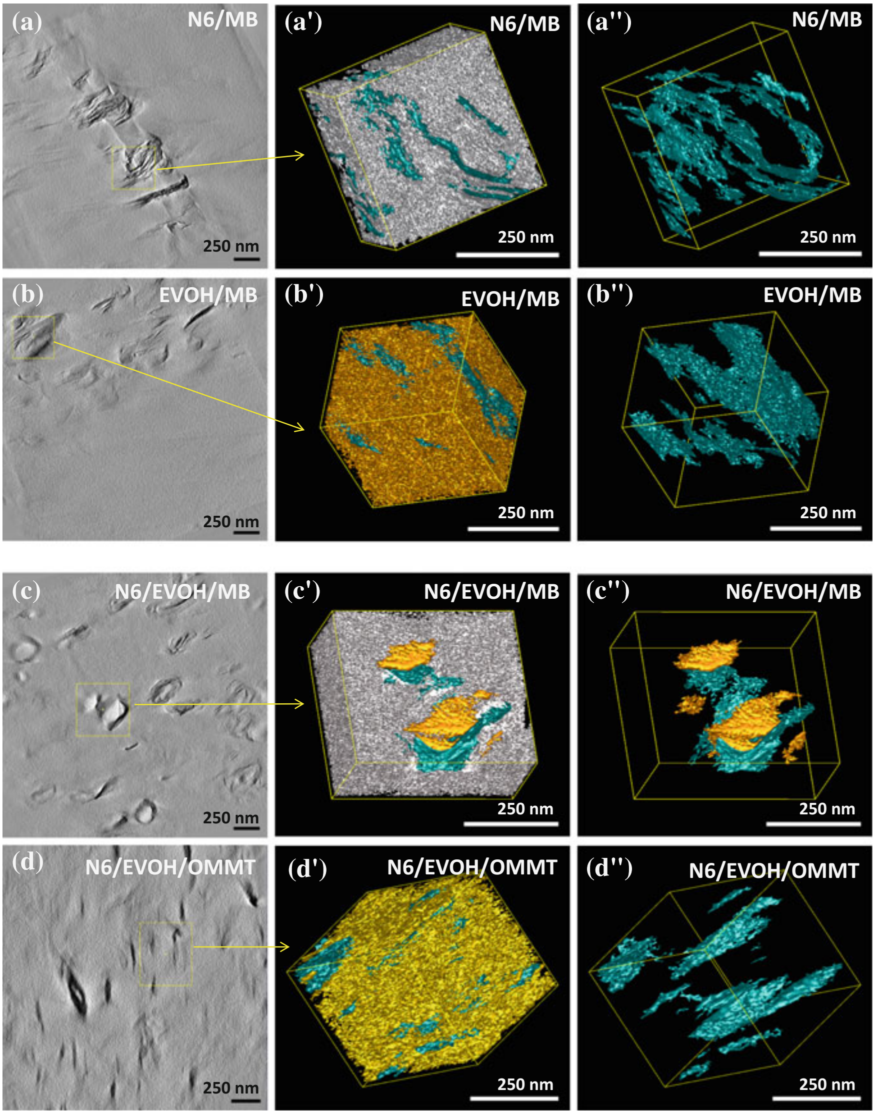

Fig. 4.14 **a–d** the 3D distributions of nanoclay platelets in the blends. The black markers represent the dispersed nanoclay particles in the blend composites. **a′–d′** and **a″–d″** the 3D projection of a selective region of 3D TEM images. Reproduced with permission from [55]. Copyright 2017, Elsevier Science Ltd

in (b) and (b′). The FTIR spectra at different positions (as indicated on the absorbance images) are shown in parts (c) and (c′). It can be seen that the absorbance was quite uniform for the PA film and it increased for the PA PNC (see Fig. 4.16). The FTIR spectra collected at two different positions (labeled 10 and 12) on the PA

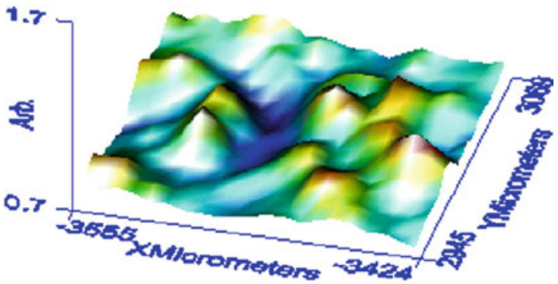
(a) PBSA/C20A nanocomposite

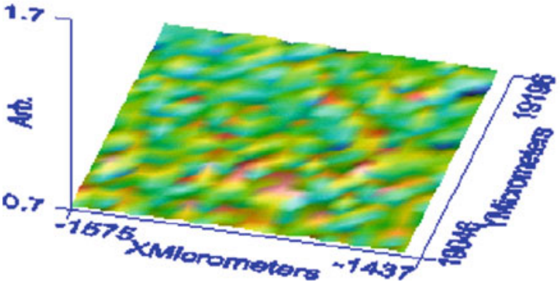
(b) PBSA/C30B nanocomposite

Fig. 4.15 Absorbance topography of **a** PBSA/C20A and **b** PBSA/C30B nanocomposites from FTIR microscopy. Reproduced with permission from [57]. Copyright 2008, Elsevier Science Ltd

film overlapped, indicating the same chemical composition (Fig. 4.16c). The results were different for PA PNC, which showed a change in the transmittance (or absorbance) when the spectra were collected at positions 13 and 15 (see Fig. 4.16c′). The reduction in certain transmission peaks was attributed to the dispersed nanoclay (Betsopa™ OM) platelets in the PA matrix. The characteristic PA peaks appeared at 3260, 2920, 1631, and 1536 cm^{-1} represented NH stretching, CH_2 stretching, amide I, and the amide II bands, respectively. The peak at 1036 confirmed the presence of the Si–O bond of the nanoclay in the PA PNC [58]. Since the spectra collected at different positions shown in Fig. 4.16b′ only differed in their intensity, it can be inferred that the nanoclays were well distributed throughout the matrix polymer. However, variations in the absorbance over the topography (Fig. 4.16a′) indicated the presence of stacked nanoclays along with well-dispersed ones.

4.4 Interfacial Analysis

Commonly used techniques, such as XRD and TEM, provide information about the inter-layer spacing of the nanoclay, but they cannot provide direct evidence on the molecular structure or the dynamics at the interface between the NP and polymer. Therefore, EPR, NMR, and dielectric spectroscopy techniques are used to investigate the interfacial regions, as discussed in this section.

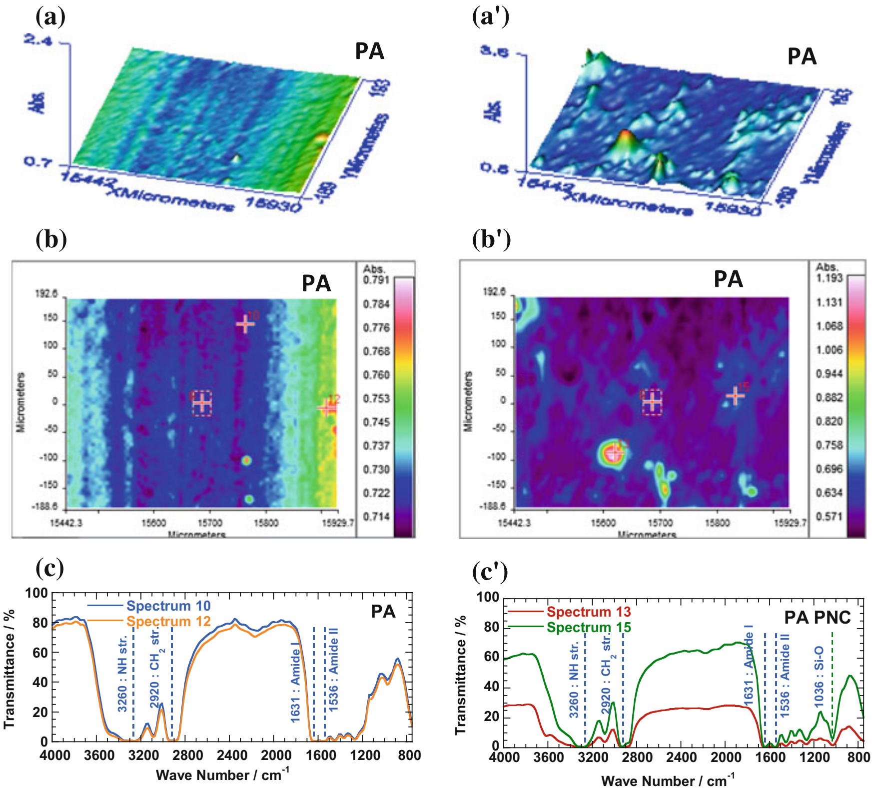

Fig. 4.16 **a**, **a′** Absorbance topography, **b**, **b′** False colour absorbance images, **c**, **c′** FTIR spectra of PA and PA PNC at different positions indicated in the absorbance images

4.4.1 Electron Paramagnetic Resonance (EPR)

It is well known that the interaction between a polymer and organically modified nanoclays plays an important role in the performance of the polymer nanocomposite. EPR techniques can be used to understand the structure and dynamics of the polymer–nanoclay interface by analyzing the surfactant layer. However, such measurements require spin labeling of the surfactant prior to organic modification of the nanoclay and use of a pre-deuterated polymer [59]. Steric acid and nitroxide molecules are commonly used for spin labeling of the surfactant, while catamine is used for spin labeling of the nanoclay surface [60]. Depending on the trans/gauche conformation, surfactant chains exhibit temperature-dependent heterogeneous mobility, as well as different dynamics along the alkyl chain [59]. These dynamics change in the PNC when polymer chains intercalate into nanoclay galleries. Electron spin echo envelope modulation (ESEEM) spectroscopy can be used to determine the anchoring position of the polymer and surfactant. For instance, Schleidt et al. [59] observed that deuterated polystyrene anchors were quite close to the middle of the surfactant chain, instead of at the end of the tail. Such information is valuable for understanding the properties of the nanocomposites.

4.4.2 *Nuclear Magnetic Resonance (NMR)*

Low-field NMR is a powerful tool for investigating the polymer dynamics and network effects in PNCs [61]. As the relaxation time is sensitive to the chemical structure, interaction process, and homogeneity, the spin lattice relaxation time (e.g., $^{13}CT_1$, $^{1}H\ T_1$) can be used to elucidate the structure and dynamics of the PNCs. The dispersed nanoclay platelets restrict the mobility of the polymer chain around the nanoclay particles [62]. Latest developments in NMR technology have enabled interpretation of the effect of the nanoclay on the chain dynamics of polymers in the PNCs under external mechanical stress and at high temperature [63]. The polymer chain dynamics can be better understood in terms of the transverse nuclear magnetic relaxation time (T_2). T_2 is affected by physical and chemical cross-linking and is measured using a Hahn Echo experiment. Böhme and Scheler [63] noticed that in a PP nanocomposite polymer–filler interaction imposed an overall restriction on the motion that extended beyond the polymer–polymer interaction. The mobile and rigid components of T_2 can be extracted from the transverse magnetization relaxation function $M(t)$ as follows [64].

$$M(t) = M_0 \exp\left[-\frac{t}{T_2^{mobile}}\right] + (1 - M_0)\exp\left[-\frac{t}{T_2^{rigid}}\right] \tag{4.47}$$

where, M_0 is the fraction of mobile chains outside the adsorption layer, and T_2^{mobile} and T_2^{rigid} are the long and short spin–spin relaxation times, respectively.

4.4.3 *Dielectric Spectroscopy*

Dielectric spectroscopy yields information about the molecular motion and relaxation process in a polymeric material subjected to an electrical field. It provides some insight into the effects of networks formed by the dispersed NPs in the matrix polymer [65]. Two major polarization mechanisms studied by dielectric spectroscopy are polarization due to orientation of dipoles and charge migrations. These responses are important for the design of optoelectronic switches, printed board circuit, fuel cells, and other devices.

In the case of PNC, interfacial interaction between the polymer chains and nanofiller (weak but numerous bonding sites) can create long-range repulsive forces between particles. Such repulsive forces influence the polarization and separation of charges [66]. The dielectric permittivity characterizes the degree of electrical polarization in the material under the influence of an external electric field. Nelson and Hu [65] noticed that a nanocomposite exhibited a higher relative permittivity as a function of frequency than its microcomposite counterpart. In addition, the change in permittivity during curing can indicate the extent of cross-linking. By knowing the permittivity, the impedance (and hence, resistance) can be calculated. The extent of reaction or degree of curing (α) can be estimated as follows [67]:

$$\frac{\alpha}{\alpha_m} = \frac{\log(\rho) - \log(\rho_0)}{\log(\rho_m) - \log(\rho_0)} \tag{4.48}$$

Here, α_m is the maximum extent of reaction, ρ_m is the corresponding resistivity, and ρ_0 and ρ are the resistivity at the initial condition and when the degree of curing reaches α, respectively. The dielectric constant (i.e., ratio of the permittivity of a material to that of air/free space) and loss as a function of frequency during isothermal curing at a particular temperature can be used to describe the dynamics related to the curing process.

The dielectric constant depends on the properties of the interfacial region in the nanocomposite [68]. For example, long chain fluoro polymer (shell) attached to the $BaTiO_2$ NP (core) results compact surface and ordered structure. As a result the molecular chain mobility of fluoro polymer chains on $BaTiO_2$ reduces. Therefore, this kind of core-shell structure of NP creates loose interfacial region when dispersed in other polymer matrix. On the other hand, short chains attached to the nanoparticle allow high molecular chain mobility and disordered structures, leading to compact interfaces in the nanocomposite. As a consequence of the compact interface, the dielectric constant increases and the dielectric loss decreases. High interfacial polarization and low dielectric loss are highly desirable for electronic and electrical applications. However, it is very challenging to fulfil such criteria in PNCs unless polarized interfacial charges effectively increase the local electrical field in the polymer matrix along the applied electric field [69]. This is possible when NPs are interconnected by forming chains, clusters, or even aggregates. Dielectric spectroscopy can be employed to investigate the segmental dynamics of multi-layered films [70]. When interpenetration of the consecutive polymer layers is negligible, the interface does not have a significant effect on the dynamics. Therefore, dielectric spectroscopy is an indirect method for interfacial analysis.

4.5 Physical Effects: Rheological, Mechanical, and Barrier Properties

The physical properties of a PNC, such as its flow behavior (rheological properties), stiffness and toughness (mechanical properties), and gas barrier performance can also be used to evaluate the structure and dispersion of NPs in the polymer matrix. The properties of the polymer depend on its inherent structure (e.g., linear, branched, or crosslinked) and crystallinity and the composition (e.g., mono-polymer or co-polymer) [71]. The shape, aspect ratio, and physical interaction between the polymer and nanofillers in the nanocomposite can produce long range connectivity or the formation of network structures [71, 72]. Any transformation in the internal structure results in changes in the flow behavior and viscoelastic properties of the nanocomposites. For instance, Fig. 4.17 shows changes in the storage/elastic (G′) and loss/viscous (G″) moduli with changes in the nanoclay content in a PBSA matrix during melt-state rheological tests. It can be seen that for PBSANC4 at high frequency, G′ dominates over G″, while frequency below 1 rad/s G″ started to dominate [73]. Such behavior is quite common as the internal structures of the nanocomposite are rigid during rapid motion (high frequency oscillations). In this state, more deformation energy can be stored and the loss of deformation energy by friction between polymer chains due to their relative motion is reduced. Thus, the elastic behavior shows increasing dominance with increasing frequency, while with decreasing frequency, the network of entanglements has sufficient time to start disentangling and hence, nanocomposite samples show increasing flexibility and mobility. At very low frequency, most of the deformation energy is lost by frictional heating effects between polymer chains due to their mutual relative motion. Such a trend was observed for changes in G′ and G″ with increasing nanoclay loading in PBSANC5 and PBSANC6. In PBSANC5, G′ and G″ superimposes on each other over a range of frequency; while in PBSANC6, G′ dominates over G″ over the entire frequency range examined. For a closely packed network system (e.g., the presence of a percolation network in a flocculated nanocomposite) minimal deformation is possible and hence, solid-like behavior dominates in PBSANC5. A further increase in the nanoclay loading (PBSANC6) restricts the mobility of polymer chains; hence, G′ dominates over G″ over the entire frequency range. Therefore, such changes in the viscoelastic properties with nanoclay loading indicate changes in the dispersion characteristics in PBSANCs. The SAXS and STEM analyses discussed above verified this interpretation of the rheological behavior for the various PBSANCs.

Usually G′ curves are used to analyze the structural strength or consistency. The effect of different kinds of structures can be distinguished, particularly in the low frequency region of frequency sweeps. Ideally, macromolecules of polymers are assumed to be linear. For such unlinked polymers, the viscoelastic properties can be explained by Maxwell’s model (a combination of spring and dashpots in series). The frequency dependence of G′ and G″ can then be obtained as follows:

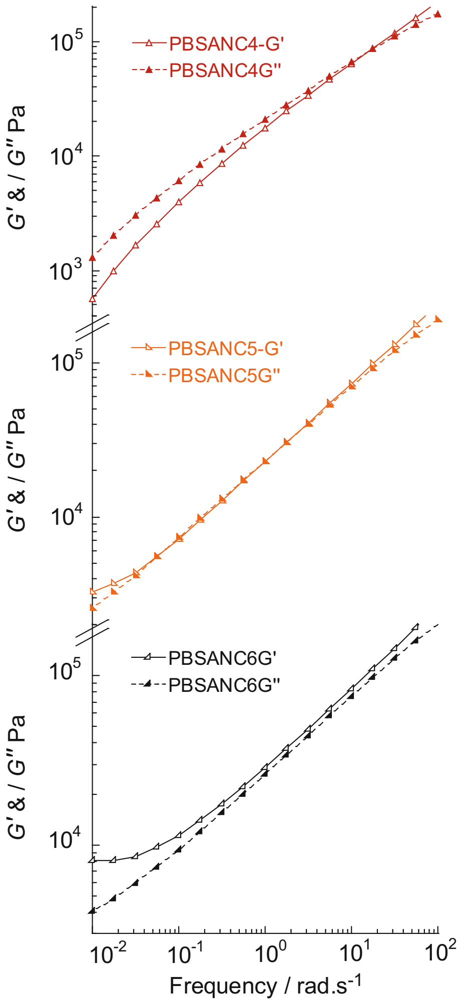

Fig. 4.17 Structural modifications observed in nanocomposites with increase in nanoclay (C30B) content. The PBSA nanocomposites with various wt% of C30B such as 4, 5, 6, were correspondingly abbreviated as PBSANC4, PBSANC5, and PBSANC6

$$G' = G_P \, . \, \frac{\omega^2\lambda^2}{\left(1 + \omega^2\lambda^2\right)} \tag{4.49}$$

$$G'' = G_P \, . \, \frac{\omega\lambda}{\left(1 + \omega^2\lambda^2\right)} \tag{4.50}$$

In a nanocomposite, the viscoelastic behavior of the polymer changes from liquid-like (i.e., G′ α ω^2 and G″ α ω from 4.49 to 4.50) to solid-like (i.e., G′ and G″ α ω^0) [74]. In Fig. 4.17, PBSANC4 shows liquid-like behavior. The solid-like behavior arises from the formation of network superstructures in PBSANC5 and then in PBSANC6 [74, 75].

PNCs exhibit enhanced structural strength, mainly due to an increased number of entanglements/network structures; the entanglements can be physical or chemical. Chemo-rheology involves the time- and temperature-dependent chemical bond formation and/or curing. Park and Jana [76] demonstrated that the elastic force exerted by cross-linked structures facilitates the dispersion of nanoclays in an epoxy matrix. It was observed that the gel temperature and time both decreased in the presence of NPs (e.g., CNTs, nanoclay) [77, 78]. Structural decomposition and regeneration (thixotropy and rheopexy) are critically important for self-healing of the polymer and nanocomposite [79, 80]. A thixotropic material exhibits a reduction in structural strength under shear force and regains the structural strength while at rest. The opposite trend is called the rheopexy. The shearing used for this purpose is high shear (above the linear viscoelastic, LVE, region) where the resting condition is simulated by the behavior in the LVE region.

Variations in the zero shear viscosity as a function of nanoclay loading can provide crucial information regarding the morphology of the blend nanocomposite. Ojijo et al. [81] elucidated the effect of nanoclay concentration on the morphology development in PLA and PBSA blends. As shown in Fig. 4.18, the authors observed a sudden increase in zero shear viscosity above 2 wt% nanoclay content. At concentrations ≤ 2 wt%, the nanoclay resided within the PBSA phase, and increased the viscosity of PLA phase only slightly. Above 2 wt% concentration, the nanoclay played an important role in controlling the zero-shear viscosity. Therefore, a disruptive change in blend morphology is expected at this point.

In addition to the flow behavior, the tensile properties, particularly the strength and elongation at break, indicated that the morphology of blend nanocomposites changed above 2 wt% nanoclay (B2; see Fig. 4.19). The authors correlated the morphology obtained from SEM analysis with the mechanical and the flow properties. Pure PLA has a much higher modulus than pure PBSA and hence, the modulus of the blend decreased significantly compared to pure PLA. However, the modulus of the composites tended to increase with increasing clay content, peaking at around 6 wt% due to the reinforcing effect of the nanoclay. However, the trends

Fig. 4.18 Zero-shear viscosity as a function of nanoclay concentration in the PLA/PBSA blend. Reproduced with permission from [81]. Copyright 2012, the American Chemical Society

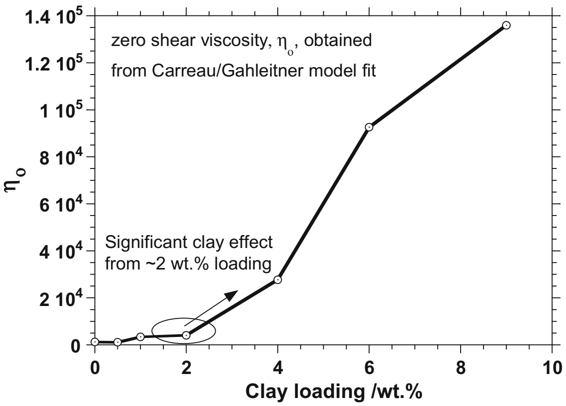

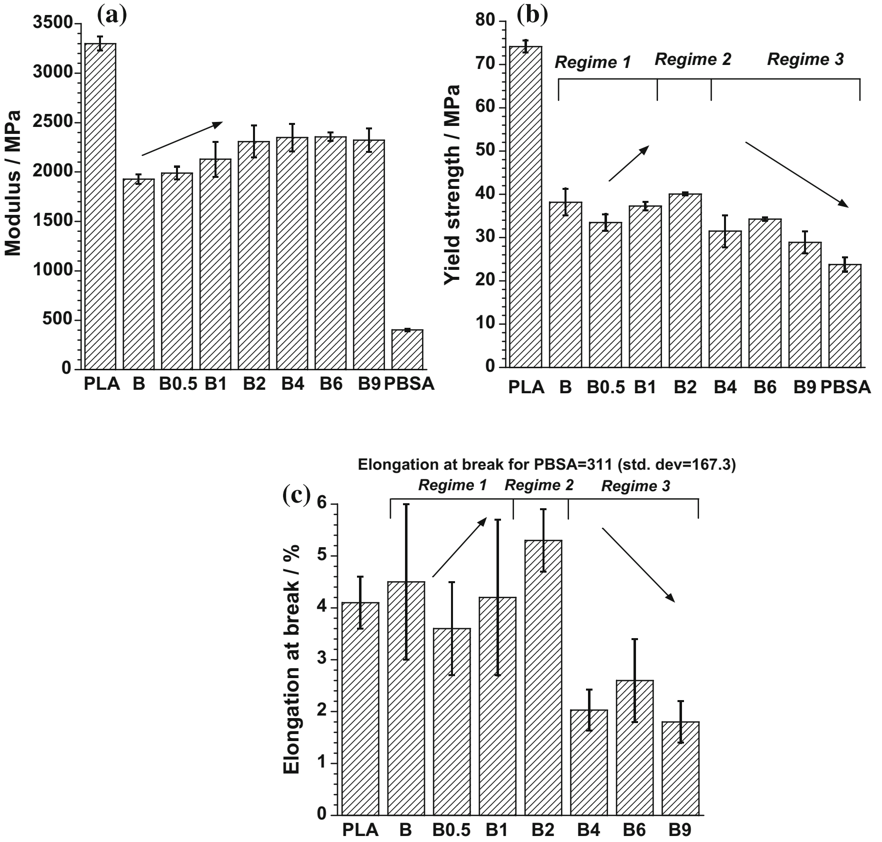

Fig. 4.19 Tensile properties of compression molded and annealed (80 °C for 12 h) samples of neat PLA, PBSA, blend (B) and blend nanocomposites (B0.5, B1, B2, B4, B6, and B9, each having 0.5, 1, 2, 4, 6, and 9 wt% of nanoclay, respectively). Reported values are averages of six independent experiments with standard deviations as error bars. The elongation at break of PBSA is 311% (std. dev. = 167.3). Reproduced with permission from [81]. Copyright 2012, the American Chemical Society

in the yield strength and elongation at break were confined to different regimes. Poor adhesion between PLA and PBSA results in a reduction in strength and elongation in the blend. A 0.5 wt% loading of nanoclay (in B0.5) seemed insufficient to affect the compatibility of the blend polymer. Increasing the nanoclay loading to 1 wt% (B1) served two purposes: stiffening the PBSA, and enhancing stress transfer between the PLA and PBSA phases due to the common adsorption of the two polymers on the clay surface. In B2 (regime 2), the nanoclays resided, not only within the PBSA phase and at the interface, but also within PLA. Hence, further improvements in the strength and elongation at break in B2 were observed.

The drastic reduction in strength and elongation at break in regime 3 of the composites was attributed to agglomeration of nanoclays in the blend matrices.

It has been shown, that in polymer nanocomposites, the interphases can occupy a significant volume fraction and influence the mechanical properties [82]. Although the Halpin-Tsai model (4.51) is commonly used to predict the mechanical performance of nanocomposites, it underpredicts the modulus in many cases.

$$E_R = \frac{1 + \eta \xi \varphi_f}{1 - \eta \varphi_f} \tag{4.51}$$

$$\eta = \left(\frac{E_f}{E_m} - 1\right) / \left(\frac{E_f}{E_m} + \xi\right) \tag{4.52}$$

Here, E_R is the ratio of the Young's modulus of the nanocomposite (E_c) to that of the matrix polymer (E_m), φ_f and E_f represent the volume fraction and modulus of the NPs, respectively.

ξ is the reinforcing factor which depends on the fiber geometry, packing geometry, and loading conditions. For a rectangular fiber cross-section with a length l and diameter d in a hexagonal array,

$$\xi = 2\left(\frac{l}{d}\right) \tag{4.53}$$

For spherical NPs, $\xi = 2$, while for circular fibers in a square array, $\xi = 1$. For a rectangular fiber with a cross-sectional area of length a and width b in a hexagonal array, $\xi = \sqrt{3}\ \ln\ (a/b)$, where a is the direction of loading. A recent study proposed that the volume fraction of the interphase (φ_i) for spherical NPs can be given by (4.54) [82].

$$\varphi_i = \left[\left(\frac{R + R_i}{R}\right)^3 - 1\right] \varphi_f \tag{4.54}$$

Here, R and R_i are the radius of NPs and the interphase thickness, respectively. By adding the interphase effect, the Halpin-Tsai model for spherical particles reduces to:

$$E_R = \frac{1 + 2\eta\varphi_f + 2\eta_i\left[\left(\frac{R+R_i}{R}\right)^3 - 1\right]\varphi_f}{1 - \eta\varphi_f - \eta_i\left[\left(\frac{R+R_i}{R}\right)^3 - 1\right]\varphi_f} \tag{4.55}$$

where,

$$\eta_f = \left(\frac{E_f}{E_m} - 1\right) / \left(\frac{E_f}{E_m} + 2\right) \tag{4.56}$$

and

$$\eta_i = \left(\frac{E_i}{E_m} - 1\right) / \left(\frac{E_f}{E_m} + 2\right) \tag{4.57}$$

Here, E_i is the Young's modulus of the interphase. Equation (4.55) accurately predicted the Young's modulus of the nanocomposites (containing spherical particles like silica, alumina, and calcium carbonate) assuming the role of the interphase [82].

It is well known that nanoclays dispersed in polymer nanocomposites impede permeating gas molecules by creating a tortuous path [83–87]. Therefore, any reduction in the gas permeation can be correlated with the extent of delamination and distribution of the nanoclays in the PNCs. The permeability of the gas molecule is estimated as the product of solubility and diffusion. Solubility is the partitioning behavior of a permeate molecule between the surface of the polymer and the surrounding headspace. Diffusion is the rate of movement of permeate molecule through the polymer matrix. According to Fick's law, the permeate flux (J) can be determined by (4.58).

$$J = -D\frac{\Delta c}{l} \tag{4.58}$$

where, D, Δc, and l represent the diffusion coefficient, change in permeate concentration, and thickness of the film, respectively.

According to Henry's law:

$$J = -D.S\frac{\Delta p}{l} \tag{4.59}$$

where, S and Δp are the ratio of equilibrium concentration of dissolved permeate to its partial pressure (c/p) and the pressure difference across the film, respectively. Combining Fick's law and Henry's law, the permeability can be written as:

$$P = D.S = \frac{J.l}{\Delta p} \tag{4.60}$$

Therefore, P is directly proportional to the permeate flux and the thickness of the film, and inversely proportional to the pressure difference across the film. D can further be correlated with the shape and size of the permeate molecule (A), free volume (f), and the minimum hole size required for a diffusion jump (B) using (4.61).

$$D = A^{-\frac{B}{f}} \tag{4.61}$$

In polymers, the glass transition temperature (T_g) is an indicator of the change in free volume. Incorporation of NPs can affect T_g and hence the gas permeability. In addition to the above-mentioned parameters, the polymer crystals and chemical structure of the polymer also play an important role in controlling the gas barrier behavior of polymeric materials. Therefore, high-aspect-ratio nanofillers and their influence on the intrinsic properties of the matrix polymer are critical parameters for enhancing the gas barrier properties of the nanocomposites.

4.6 Conclusion

The techniques described in this chapter are complementary to each other. While microscopy allows direct visualization of dispersed nanoparticles over a small area, X-ray scattering analyzes the overall dispersion and distribution characteristics, degree of anisotropy in the system, and crystal structures. However, these methods cannot provide direct evidence on the molecular structure or the dynamics of the interface. Electron paramagnetic resonance, nuclear magnetic resonance, and dielectric spectroscopy allow investigation of the interfacial regions. Other indirect measurements for evaluating the structure of the nanocomposites include rheological (studying the flow behavior), mechanical, and gas diffusion tests.

Acknowledgements The authors would like to thank the Department of Science and Technology and the Council for Scientific and Industrial Research, South Africa, for financial support.

References

1. Drummy LF, Wang YC, Schoenmakers R, May K, Jackson M, Koerner H, Farmer BL, Mauryama B, Vaia RA. Morphology of layered silicate- (nanoclay-) polymer nanocomposites by electron tomography and small-angle X-ray scattering. Macromolecules. 2008;41:2135–43.
2. Ho DL, Briber RM, Glinka CJ. Characterization of organically modified clays using scattering and microscopy techniques. Chem Mater. 2001;13:1923–31.
3. Mittelbach R, Glatter O. Direct structure analysis of small-angle scattering data from polydisperse colloidal particles. J Appl Crystallogr. 1998;31:600–8.
4. Schnablegger H, Singh Y. A practical guide to small angle X-ray scattering. Austria: Anton Par GmbH; 2006.
5. Glatter O, Kratky O. Small angle X-ray scattering. London: Academic Press; 1982. ISBN 0-12-286280-5.
6. Glatter O. Data evaluation in small angle scattering: calculation of the radial electron density distribution by means of indirect Fourier transformation. Acta Phys Austriaca. 1977;47:83–102.
7. Glatter O. A new method for the evaluation of small-angle scattering data. J Appl Crystallogr. 1977;10:415–21.

8. Bergmann A, Fritz G, Glatter O. Solving the generalized indirect Fourier transformation (GIFT) by Boltzmann simplex simulated annealing (BSSA). J Appl Crystallogr. 2000;33:1212–6.
9. Brunner-Popela J, Glatter O. Small-angle scattering of interacting particles. I. Basic principles of a global evaluation technique. J Appl Crystallogr. 1997;30:431–42.
10. Weyerich B, Brunner-Popela J, Glatter O. Small-angle scattering of interacting particles. II. Generalized indirect Fourier transformation under consideration of the effective structure factor for polydisperse systems. J Appl Crystallogr. 1999;32:197–209.
11. Hosemann R, Bagchi SN. Direct analysis of diffraction by matter. Amsterdam, The Netherlands: North-Holland; 1962.
12. Guinier A. X-ray diffraction in crystals, imperfect crystals and amorphous bodies. Ontario, Canada: General Publishing Company; 1994.
13. Caillé A, Seances CR. Remarks on the scattering of X-rays by A-type smectics. Actes Soc Hist B. 1972;274:891–3.
14. Zhang R, Tristram-Nagle S, Sun W, Headrick RL, Irving TC, Suter RM, Nagle JF. Small-angle X-ray scattering from lipid bilayers is well described by modified Caillé theory but not by paracrystalline theory. Biophys J. 1996;70:349–57.
15. Zhang R, Suter RM, Nagle JF. Theory of the structure factor of lipid bilayers. Phys Rev E. 1994;50:5047–60.
16. Frühwirth T, Fritz G, Freiberger N, Glatter O. Structure and order in lamellar phases determined by small-angle scattering. J Appl Crystallogr. 2004;37:703–10.
17. Glatter O. Convolution square root of band-limited symmetrical functions and its application to small-angle scattering data. J Appl Crystallogr. 1981;14:101–8.
18. Glatter O, Hainisch B. Improvements in real-space deconvolution of small-angle scattering data. J Appl Crystallogr. 1984;17:435–41.
19. Glatter O. Comparison of two different methods for direct structure analysis from small-angle scattering data. J Appl Crystallogr. 1988;21:886–90.
20. Li TC, Ma J, Wang M, Tjiu C, Liu T, Huang W. Effect of clay addition on the morphology and thermal behaviour of polyamide 6. J Appl Polym Sci. 2007;103:1191–9.
21. Ganguli A, Bhowmick AK. Insights into montmorillonite nanoclay based ex situ nanocomposites from SEBS by small angle X-ray scattering and modulated DSC studies. Macromolecules. 2008;41:6246–53.
22. Preschilla N, Sivalingam G, Rasheed AS, Tyagi S. Quantification of organoclay dispersion and lamellar morphology in poly(propylene) nanocomposites with small angle X-ray scattering. Polymer. 2008;49:4285–97.
23. Nawani P, Burger C, Chu B, Hsiao BS, Tsou AH, Weng W. Characterization of nanoclay orientation in polymer nanocomposite film. Polymer. 2010;51:5255–66.
24. Bandyopadhyay J, Ray SS. The quantitative analysis of nano-clay dispersion in polymer nanocomposites by small angle X-ray scattering combined with electron microscopy. Polymer. 2010;51:1437–49.
25. Carli LN, Bianchi O, Machado G, Crespo JS, Mauler RS. Morphological and structural characterization of PHBV/organoclay nanocomposites by small angle X-ray scattering. Mater Sci Eng. 2013;33:932–7.
26. Yadav R, Naebe M, Wang X, Kandasubramanian B. Structural and thermal stability of polycarbonate decorated fumed silica nanocomposite via thermomechanical analysis and in-situ temperature assisted SAXS. Sci Rep. 2017;7:7706. https://doi.org/10.1038/s41598-017-08122-7.
27. Jouault N, Dalmas F, Boúe F, Jestin J. Multiscale characterization of filler dispersion and origins of mechanical reinforcement in model nanocomposites. Polymer. 2012;53:761–75.
28. Bandyopadhyay J, Malwela T, Ray SS. Study of change in dispersion and orientation of clay platelets in a polymer nanocomposite during tensile test by variostage small-angle X-ray scattering. Polymer. 2012;53:1747–59.

29. Bandyopadhyay J, Ray SS. Determination of structural changes of dispersed clay platelets in a polymer blend during solid-state rheological property measurement by small-angle X-ray scattering. Polymer. 2011;52:2628–42.
30. Gurun B, Bucknall DG, Thio YS, Teoh CC, Harkin-Jones E. Multiaxial deformation of polyethylene and polyethylene/clay nanocomposites: in situ synchrotron small angle and wide angle X-ray scattering study. J Polym Sci Part B Polym Phys. 2011;49:669–77.
31. Nishada T, Obayashi A, Haraguchi K, Shibayama M. Stress relaxation and hysteresis of nanocomposite gel investigated by SAXS and SANS measurement. Polymer. 2012;53:4533–8.
32. Bandyopadhyay J, Sinha Ray S, Scriba M, Wesley-Smity J. A combined experimental and theoretical approach to establish the relationship between shear force and clay platelet delamination in melt-processed polypropylene nanocomposites. Polymer. 2014;55:2233–45.
33. Pujari S, Dougherty L, Mobuchon C, Carreau PJ, Heuzey M-C, Burghardt WR. X-ray scattering measurements of particle orientation in a sheared polymer/clay dispersion. Rheol Acta. 2011;50:3–16.
34. Thompson A, Bianchi O, Amorim CLG, Lemos C, Teixeira SR, Samios D, Giacomelli C, Crespo JS, Machado G. Uniaxial compression and stretching deformation of an i-PP/EPDM/organoclay nanocomposite. Polymer. 2011;52:1037–44.
35. Yamashita M, Kato M. Lamellar crystal thickness transition of melt crystallized isotactic polybutene-1 observed by small-angle X-ray scattering. J Appl Crystallogr. 2007;40:s650–5.
36. Fu Q, Heck B, Strobl G, Thoman Y. A temperature- and molar mass-dependent change in the crystallization mechanism of poly(1-butene): transition from chain-folded to chain-extended crystallization? Macromolecules. 2001;34:2502–11.
37. Marega C, Causin V, Saini R, Marigo A. A direct SAXS determination of specific surface area of clay in polymer-layered silicate nanocomposites. J Phys Chem B. 2012;116:7596–602.
38. Bunge HJ. Influence of texture on powder diffraction. Text Microstruct. 1997;29:1–26.
39. Courgneau C, Domenek S, Lebossé R, Guinault A, Avérous L, Ducruet V. Effect of crystallization on barrier properties of formulated polylactide. Polym Int. 2012;62:180–9.
40. Incarnato L, Scarfato P, Russo GM, Maio LD, Iannelli P, Acierno D. Preparation and characterization of new melt compounded copolyamide nanocomposites. Polymer. 2003;44:4625–34.
41. Zhu W, Chen T, Li Y, Lei J, Chen X, Yao W, Duan T. High performances of artificial nacre-like graphene oxide-carrageenan bio-nanocomposite films. Materials. 2017;10:536. https://doi.org/10.3390/ma10050536.
42. Hikku GS, Jeyasubramanian K, Venugopal A, Ghosh R. Corrosion resistance behaviour of graphene/polyvinyl alcohol nanocomposite coating for aluminium-2219 alloy. J Alloy Compd. 2017;716:259–69.
43. Maravi S, Bajpai J, Bajpai AK. Improving mechanical and electrical properties of poly(vinyl alcohol-*g*-acrylic acid) nanocomposite films by reinforcement of thermally reduced graphene oxide. Polym Sci Ser A. 2017;59:751–63.
44. Di Mauro A, Cantarella M, Nicotra G, Pellegrino G, GulinonA Brundo MV, Privitera V, Impellizzeri G. Novel synthesis of ZnO/PMMA nanocomposites for photocatalytic application. Sci Rep. 2017;7:40895. https://doi.org/10.1038/srep40895.
45. Shanthala VS, Devi SN, Murugendrappa MV. Synthesis, characterization and DC conductivity studies of polypyrrole/copper zinc iron oxide nanocomposites. J Asian Ceram Soc. 2017;5:227–34.
46. Vaez M, Alijini S, Omidkhah M, Moghaddam AZ. Synthesis, characterization and optimization of N-TiO_2/PANI nanocomposite for photodegradation of acid dye under visible light. Polym Compos. 2017. https://doi.org/10.1002/pc.24574.
47. Chen Y-H, Zhong GJ, Wang Y, Li ZM, Li L. Unusual tuning of mechanical properties of isotactic polypropylene using counteraction of shear flow and β-nucleating agent on β-form nucleation. Macromolecules. 2009;42:4343–8.
48. Zhang Y-F, Chang Y, Li X, Xie D. Nucleation effects of a novel nucleating agent bicyclic [2,2,1]heptane di-carboxylate in isotactic polypropylene. J Macromol Sci. 2011;50:266–74.

49. De Santis F, Pantani R. Optical properties of polypropylene upon recycling. Sci World J. 2013;2013:1–7.
50. Malas A, Bharati A, Verkinderen O, Goderis B, Moldenaers P, Cardinaels R. Effect of the GO reduction method on the dielectric properties, electrical conductivity and crystalline behavior of PEO/rGO nanocomposites. Polymers. 2017;9:613. https://doi.org/10.3390/polym9110613.
51. Nwofe PA, Ramakrishna Reddy KT, Sreedevi G, Tan JK, Forbes I, Miles RW. Single phase, large grain, p-Conductivity-type SnS layers produced using the thermal evaporation method. Energy Proc. 2012;15:354–60.
52. Wang Y, Tang W, Zhang L. Crystalline size effects on texture coefficient, electrical and optical properties of sputter-deposited Ga-doped ZnO thin films. J Mater Sci Technol. 2015;31:175–81.
53. Ilican S, Caglar M, Caglar Y. Determination of the thickness and optical constants of transparent indium-doped ZnO thin films by the envelope method. Mater Sci Pol. 2007;25:709–18.
54. Bandyopadhyay J, Sinha Ray S. Mechanism of enhanced tenacity in a polymer nanocomposite studied by small-angle X-ray scattering and electron microscopy. Polymer. 2010;51:4860–6.
55. Bandyopadhyay J, Sinha Ray S, Salehiyan R, Ojijo V. Effect of the mode of nanoclay inclusion on morphology development and rheological properties of nylon6/ethyl-vinyl-alcohol blend composites. Polymer. 2017;126:96–108.
56. Bhargava R, Wang S-Q, Koenig JL. FTIR microscopy of the polymeric systems. Adv Polym Sci. 2003;163:137–91.
57. Ray SS, Bandyopadhyay J, Bousmina M. Influence of degree of intercalation on the crystal growth kinetics of poly[(butylene succinate)-co-adipate] nanocomposites. Eur Polymer J. 2008;44:3133–3145.
58. Alabarse FG, Conceição RV, Balzaretti NM. In-situ FTIR analyses of bentonite under high-pressure. Appl Clay Sci. 2011;51:202–8.
59. Schleidt S, Spiess HW, Jeschke G. A site-directed spin-labeling study of surfactants in polymer–clay nanocomposites. Colloid Polym Sci. 2006;284:1211–9.
60. Kielmann U, Jeschke G, García-Rubio G. Structural characterization of polymer-clay nanocomposites prepared by co-precipitation using EPR techniques. Materials. 2014;7:1384–408.
61. Papon A, Saalwächter K, Schäler K, Guy L, Montes H. Low-field NMR investigations of nanocomposites: polymer dynamics and network effects. Macromolecule. 2011;44:913–22.
62. da Silva E, Tavares MIB, Nogueira JS. Solid state evaluation of natural resin/clay nanocomposites. J Nano Res. 2008;4:117–26.
63. Böhme U, Scheler U. Interfaces in polymer nanocomposites—an NMR study. Proceedings of PPS-31. AIP Conf Proc. 2016;1713:090009-1–3.
64. Dewimille L, Bresson B, Bokobza L. Synthesis, structure and morphology of poly(dimethylsiloxane) networks filled with in situ generated silica particles. Polymer. 2005;46:4135–43.
65. Nelson JK, Hu Y. Nanocomposite dielectrics—properties and implications. J Phys D Appl Phys. 2005;38:213–22.
66. Lewis TJ. Interfaces: nanometric dielectrics. J Phys D Appl Phys. 2005;38:202–12.
67. Kenny JM, Trivisano A. Isothermal and dynamic reaction kinetics of high performance epoxy matrices. Polym Eng Sci. 1991;31:1426–33.
68. Wang K, Huang X, Huang Y, Xie L, Jiang P. Fluoro-polymer@$BaTiO_3$ hybrid nanoparticles prepared via RAFT polymerization: Toward ferroelectric polymer nanocomposites with high dielectric constant and low dielectric loss for energy storage application. Chem Mater. 2013;25:2327–38.
69. Zhang G, Brannum D, Dong D, Tang L, Allahyarov E, Tang S, Kodweis K, Lee J-K, Zhu L. Interfacial polarization-induced loss Mechanisms in polypropylene/$BaTiO_3$ nanocomposite dielectrics. Chem Mater. 2016;28:4646–60.

70. Casalini R, Prevosto D, Labardi M, Roland CM. Effect of interface interaction on the segmental dynamics of poly(vinyl acetate) investigated by local dielectric spectroscopy. ACS Macro Lett. 2015;4:1022–6.
71. Abraham J, Sharika T, George SC, Thomas S. Rheological percolation in thermoplastic polymer nanocomposites. Rheol Open Access. 2017;1:1–15.
72. Knauret ST, Douglas JF, Starr FW. The effect of nanoparticle shape on polymer-nanocomposite rheology and tensile strength. J Polym Sci Part B Polym Phys. 2007;45: 1882–97.
73. Bandyopadhyay J, Ray SS, Maiti A, Khatua B. Thermal and rheological properties of biodegradable poly[(butylene succinate)-co-adipate] nanocomposites. J Nanosci Nanotechnol. 2010;10:4184–95.
74. Krishnamoorti R, Yurekli K. Rheology of polymer layered silicate nanocomposites. Curr Opin Colloid Interface. 2001;6:464–70.
75. Eslami H, Grmela M, Bousmina M. A mesoscopic tube model of polymer/layered silicate nanocomposites. Rheol Acta. 2009;48:317–31.
76. Park JH, Jana SC. Mechanism of exfoliation of nanoclay particles in epoxy-clay nanocomposites. Macromolecules. 2003;36:2758–68.
77. Terenzi A, Vedova C, Leilli G, Mijovic J, Torre L, Valentini L, Kenny JM. Chemorheological behaviour of double-walled carbon nanotube-epoxy nanocomposites. Compos Sci Technol. 2008;68:1862–8.
78. Kim J-T, Martin D, Halley P, Kim DS. Chemorheological studies on a thermoset PU/clay nanocomposite system. Compos Interfaces. 2012;14:449–65.
79. Fox J, Wie J, Greenland B, Burattini S, Hayes W, Colquhoun H, Mackay M, Rowan S. High strength, healable, supramolecular polymer nanocomposites. J Am Chem Soc. 2012;134: 5362–8.
80. Wang Y, He J, Aktas S, Sukhishvilli SA, Kalyon DM. Rheological behaviour and self-healing of hydrogen-bonded complexes of a tribock Pluronic® copolymer with weak polyacid. J Rheol. 2017;61:1103. https://doi.org/10.1122/1.4997591.
81. Ojijo V, Ray SS, Sadiku R. Effect of nanoclay loading on the thermal and mechanical properties of biodegradable polylactide/poly[(butylene succinate)-co-adipate] blend composites. ACS Appl Mater Interfaces. 2012;4:2395–405.
82. Zare Y. Development of Halpin-Tsai model for polymer nanocomposites assuming interphase properties and nanofiller size. Polym Test. 2016;51:69–73.
83. Arunvisut S, Phummanee S, Somwangthanaroj A. Effect of clay on mechanical and gas barrier properties of blown film LDPE/clay nanocomposites. J Appl Polym Sci. 2007;106:2210–7.
84. Golebiewski J, Rozanski A, Dzwonkowski J, Galeski A. Low density polyethylene–montmorillonite nanocomposites for film blowing. Eur Polymer J. 2008;44:270–86.
85. Lotti C, Isaac CS, Branciforti MC, Alves RM, Liberman S, Bretas RE. Rheological, mechanical and transport properties of blown films of high density polyethylene nanocomposites. Eur Polymer J. 2008;44:1346–57.
86. Yeh J-T, Chang C-J, Tsai F-C, Chen K-N, Huang K-S. Oxygen barrier and blending properties of blown films of blends of modified polyamide and polyamide-6 clay mineral nanocomposites. Appl Clay Sci. 2009;45:1–7.
87. Garofalo E, Fariello ML, Di Maio L, Incarnato L. Effect of biaxial drawing on morphology and properties of copolyamide nanocomposites produced by film blowing. Eur Polymer J. 2013;49:80–9.